



1  
2 **The response of sea ice and high salinity shelf water in the Ross Ice Shelf Polynya to cyclonic**  
3 **atmosphere circulations**

4 **Xiaoqiao Wang<sup>1</sup>, Zhaoru Zhang<sup>1 2\*</sup>, Michael S. Dinniman<sup>3</sup>, Petteri Uotila<sup>4</sup>, Xichen Li<sup>5</sup>, Meng Zhou<sup>1</sup>**  
5 **<sup>2</sup>**

6 <sup>1</sup> School of Oceanography, Shanghai Jiao Tong University, Shanghai, China.

7 <sup>2</sup> Key Laboratory for Polar Science, Polar Research Institute of China, Ministry of Natural Resources,  
8 200136, Shanghai.

9 <sup>3</sup> Center for Coastal Physical Oceanography, Old Dominion University, Norfolk, VA 23529, USA.

10 <sup>4</sup> Institute for Atmospheric and Earth System Research/Physics, Faculty of Science, University of  
11 Helsinki, Helsinki, Finland.

12 <sup>5</sup> International Center for Climate and Environment Sciences, Institute of Atmospheric Physics, Chinese  
13 Academy of Sciences, Beijing, China.

14

15 Corresponding author: Zhaoru Zhang ([zrzhang@sjtu.edu.cn](mailto:zrzhang@sjtu.edu.cn))

16

17

18 **Abstract**

19 Coastal polynyas in the Ross Sea are important source regions of high salinity shelf water (HSSW) – the  
20 precursor of Antarctic Bottom Water that supplies the lower limb of the thermohaline circulation. Here, the  
21 response of sea ice production and HSSW formation to synoptic- and meso-scale cyclones were  
22 investigated for the Ross Ice Shelf Polynya (RISP) using a coupled ocean-sea ice-ice shelf model targeted  
23 on the Ross Sea. When synoptic-scale cyclones prevailed over RISP, sea ice production (SIP) increased  
24 rapidly by 20–30% over the entire RISP. During the passage of mesoscale cyclones, SIP increased by about  
25 2 times over the western RISP but decreased over the eastern RISP, resulting respectively from  
26 enhancement in the offshore and onshore winds. HSSW formation mainly occurred in the western RISP  
27 and was enhanced responding to the SIP increase under both types of cyclones. Promoted HSSW formation  
28 could persist for 12–48 hours after the decay of the cyclones. The HSSW export across the Drygalski  
29 Trough was negatively correlated with the meridional wind speed, while the export across the Glomar  
30 Challenger Trough was positively correlated with the meridional wind. Such correlations are mainly  
31 controlled by variations in geostrophic ocean currents that result from sea surface elevation change.  
32



## 33 1 Introduction

34 Antarctic coastal polynyas are characterized by the areas of persistent open water surrounded by sea ice  
35 along the coastlines, which tend to appear recurrently at fixed geographical locations and periods of the  
36 year. These coastal polynyas are mechanically driven by offshore katabatic and synoptic winds (Bromwich  
37 et al., 1998; Massom et al., 1998; Morales Maqueda et al., 2004). Katabatic wind is traditionally defined as  
38 a downslope cold flow driven by gravity and pressure gradient force over a sloping surface near the  
39 Antarctic coast, and its direction is largely controlled by local topography (Lutgens and Tarbuck, 2001). In  
40 general, the near-surface wind fields over the Antarctic continent are forced by both katabatic flow and  
41 meso- or synoptic-scale atmospheric forcing. New sea ice production within coastal polynyas and the  
42 associated brine rejection process leads to the formation of high salinity shelf water (HSSW), which is a  
43 precursor of Antarctic Bottom Water (AABW), a key component of the lower cell of the meridional  
44 overturning circulation (Comiso and Gordon, 1998; Ohshima et al., 2013; Whitworth et al., 2013).  
45 Furthermore, Antarctic coastal polynyas are identified as biological “hot spots” due to the enhanced primary  
46 productivity during the austral spring and summer (Arrigo and van Dijken, 2003). The polynya regions are  
47 also characterized by massive atmospheric CO<sub>2</sub> sinking (Hoppema and Anderson, 2007; Arrigo et al., 2008;  
48 Tortell et al., 2012) resulting from deep convection and large amounts of phytoplankton accumulation  
49 compared with adjacent waters (Tremblay and Smith, 2007). Consequently, coastal polynya processes play  
50 an important role in the global climate system.

51

52 Previous studies indicate that the sea ice production rate (SIP) and HSSW formation within the coastal  
53 polynyas are significantly increased with the strength of katabatic winds (Mathiot et al., 2010; Barthélemy  
54 et al., 2012; Zhang et al., 2015; Dale et al., 2017; Cheng et al., 2019). Most of these studies focused on the  
55 role of winds in the Antarctic coastal polynyas on seasonal or longer time scales. However, atmospheric  
56 conditions along the Antarctic coast are characterized by high-frequency wind events associated with the  
57 passages of synoptic- or mesoscale cyclones (Turner et al., 2009; Chenoli et al., 2015; Weber et al., 2016;  
58 Wang et al., 2021). The coastal margin of Antarctica is regarded as the most active cyclogenetic region on  
59 earth due to the existence of a strong baroclinic zone around the Antarctic continent (Parish and Cassano,  
60 2003). The coastal Ross Sea, which has been identified as an important source region of AABW due to the  
61 presence of the Terra Nova Bay and the Ross Ice Shelf polynyas (Jacobs et al., 1970; Gordon and Comiso,  
62 1988; Whitworth and Orsi, 2006), is frequently affected by the passages of cyclones (Bromwich et al., 1993;  
63 Simmonds et al., 2003; Knuth et al., 2011; Uotila et al., 2011; Yu et al., 2019). Recent studies have begun  
64 to focus on the influence of synoptic-scale wind forcing on sea ice properties in the Ross Sea polynyas  
65 based on the observations. The sea ice properties and the polynya extent have a strong correlation with  
66 wind speed in the Ross Sea polynyas (Dale et al., 2017; Cheng et al., 2019; Ding et al., 2020). Thompson  
67 et al. (2020) demonstrated using in-situ observations, available from the Polynyas and Ice Production and  
68 seasonal Evolution in the Ross Sea (PIPERS) program which conducted an autumn ship campaign in 2017  
69 and two spring airborne campaigns in 2016 and 2017, that the estimated frazil ice production could increase  
70 up to 110 cm d<sup>-1</sup> during the strongest wind events (Ackley et al., 2020). Wenta and Cassano (2020) found  
71 that during an extreme wind event associated with the passage of two cyclones, the extent of the Terra Nova  
72 Bay polynya (TNB) increased dramatically by over 20-fold. These studies provide important insights into  
73 the response of polynyas to changes in atmospheric forcing. However, the influence of cyclones on the  
74 oceanic processes, including the convection and the formation of HSSW that directly affect the AABW and  
75 thermohaline circulation, has not been revealed. Moreover, different types and paths of cyclones may  
76 induce different coastal wind patterns over the polynyas, and result in distinct responses by sea ice  
77 production and the HSSW formation. The extent of these processes remains uncertain but would be  
78 important for understanding the short-scale variability of HSSW and even the AABW formation.

79



80 As very few in-situ measurements have been conducted at the Antarctic coastal polynyas during the  
81 freezing season, numerical models have become indispensable methods to investigate the response of sea  
82 ice and oceanic processes to harsh weather conditions, such as cyclones. In this study, a 5-km resolution  
83 regional ocean-sea ice-ice shelf model for the Ross Sea was employed to investigate the role of meso- and  
84 synoptic-scale cyclones in sea ice production and the HSSW formation in the Ross Ice Shelf polynya (RISP),  
85 which is the largest coastal polynya with the highest SIP over the Southern Ocean (Tamura et al., 2008;  
86 Kern et al., 2009). This manuscript is organized as follows. In Section 2, descriptions of the numerical  
87 model, observational data, and model validation and analysis methods are provided. In Section 3, the  
88 impacts of different types of cyclones on the variations of sea ice production and water mass formation are  
89 presented and interpreted. Discussions on the HSSW exports in the troughs that are major conduits for  
90 HSSW outflow and their relationship with the meridional winds are given in section 4. Section 5 provides  
91 the summary and conclusions.

92

## 93 **2 Date and Methods**

### 94 **2.1 Model data description**

95 This study utilizes the Ross Sea circulation model as described in Dinniman et al. (2018), which is  
96 implemented with the Regional Ocean Modeling System (ROMS). ROMS combines a primitive-equation,  
97 finite-volume ocean model with a dynamic sea ice model (Budgell, 2005) based on an elastic-viscous-  
98 plastic (EVP) rheology solver (Hunke and Dukowicz, 1997; Hunke, 2001). The sea ice model applies the  
99 two-layer ice thermodynamics following Mellor and Kantha (1989) and Häkkinen and Mellor (1992),  
100 which has been verified that it can well simulate sea ice variables over coastal regions around the Antarctic  
101 including the Ross Sea (Stern et al., 2013; Dinniman et al., 2011, 2015). The ice shelves used in this model  
102 are static, which means that the motion or mass change of the ice sheet, including iceberg calving, is ignored.  
103 The thermodynamic and mechanical effects of the Ross Ice Shelf (RIS) cavity on the adjacent water beneath  
104 are parameterized (Holland and Jenkins, 1999; Dinniman et al., 2011). The momentum, heat, and  
105 freshwater (imposed as a salt flux) fluxes in the open ocean are calculated from the COARE version 3.0  
106 bulk flux formulae (Fairall et al., 2003). There is no relaxation for surface temperature or salinity towards  
107 prescribed values, such as an observational climatology.

108

109 The southern extent of the Ross Sea model domain includes most of the cavity under the RIS, and the  
110 northernmost part consists of the continental shelf break and extends to 67.5°S (Fig. 1). The model has a  
111 horizontal resolution of 5 km, and 24 vertical layers with variable thicknesses (higher resolution towards  
112 the top and bottom surfaces) based on a terrain-following vertical coordinate system (Haidvogel et al., 2008;  
113 Shchepetkin and McWilliams, 2009). The topographic datasets used in this model are from the International  
114 Bathymetric Chart of the Southern Ocean (IBCSO) and Bedmap2 (Arndt et al., 2013; Fretwell et al., 2013)  
115 which include the elevation of the bedrock and the base of any floating ice shelves (mainly for the RIS).  
116 The lateral open boundary conditions for temperature and salinity are derived from the climatological data  
117 based on the World Ocean Atlas 2001 (WOA01), and for barotropic velocities from the Ocean Circulation  
118 and Climate Advanced Modelling project (OCCAM; Saunders et al., 1999). Monthly observed data from  
119 passive microwave satellite observations (SSM/I) over 1999–2014 are used as the lateral open boundaries  
120 for sea ice concentration. Ocean tidal currents and the inverse barometer effect are not included. Monthly  
121 climatological precipitation used in this model is derived from the Antarctic Mesoscale Prediction System  
122 (AMPS), a high-resolution atmospheric model over the Antarctic (Powers et al., 2003; Bromwich et al.,  
123 2005). Monthly cloud fraction climatology data comes from the International Satellite Cloud Climatology  
124 Project stage D2 (ISCCP D2; Rossow et al., 1996), which is used to calculate net longwave and shortwave  
125 radiations following Berliand (1952). Other atmospheric forcing fields including 6-hourly winds and air  
126 temperature and monthly sea level pressure and humidity, were obtained from the ERA-Interim reanalysis

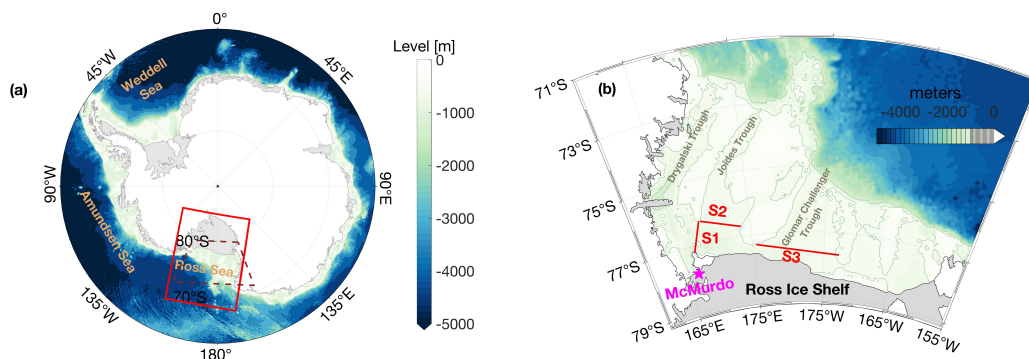


127 product (Dee et al., 2011) produced by the European Centre for Medium-Range Weather Forecasts  
128 (ECMWF) (Dinniman et al., 2018). These atmospheric variables are used in the bulk formulae to generate  
129 the surface fluxes in the Ross Sea model (Fairall et al., 2003). The ERA-Interim has a spectral T255  
130 horizontal resolution which corresponds to approximately 79 km spacing on a reduced Gaussian grid. The  
131 ERA-Interim reanalysis products can well resolve the meso- and synoptic-scale cyclones (Uotila et al.,  
132 2013; Chenoli et al., 2015; Yu et al., 2019). The Ross Sea model simulation spans from 15 September 1999  
133 to 15 September 2014 after a 6-yr spin-up simulation, and the model results are output as 5-day-average  
134 values. In this study, for the selected periods of synoptic-scale or mesoscale atmospheric events, model  
135 simulations over June to September of 2005 and 2014 are output as 6-hourly results, which is essential to  
136 revealing the detailed processes over the short duration of the cyclone events.

137

## 138 2.2 Observational data for model validation

139 In this work, the simulated sea ice concentration in the RISP was validated by the daily Bootstrap Sea Ice  
140 Concentrations from Nimbus-7 SMMR and DMSP SSM/I-SSMIS archived at the National Snow and Ice  
141 Data Center (NSIDC) (Markus and Cavalieri, 2000; Comiso, 2017), which have a horizontal resolution of  
142 25 km (<https://nsidc.org/data/nsidc-0079/versions/3>). The Advanced Microwave Scanning Radiometer-  
143 Earth Observing System (AMSR-E) product derived SIP was employed to evaluate the modelled SIP. The  
144 AMSR-E SIP is estimated based on the heat flux calculation using a thin-ice-thickness estimation algorithm  
145 and surface atmospheric data (<http://wwwod.lowtem.hokudai.ac.jp/polar-seaflux>), assuming that the  
146 contribution of oceanic heat flux to sea-ice freezing/melting process is negligible (Nihashi and Ohshima,  
147 2015; Nihashi et al., 2017). The AMSR-E SIP dataset was calculated over 2003–2010, and the annual  
148 cumulative SIP is defined as the integrated ice production from March to October, i.e. the freezing season  
149 (Nihashi and Ohshima, 2015). Wind speeds at 10 m from the ERA-Interim reanalysis were compared with  
150 measured 10-m wind data at the McMurdo Station near the Ross Island (Fig. 1b) over austral winter. The  
151 wind speed data are available at the Reference Antarctic Data for Environmental Research (READER)  
152 project website (<http://legacy.bas.ac.uk/met/READER>). We selected two winters to study the influence of  
153 cyclone events, which are featured by high correlations between wind speed from ERA-Interim and  
154 observations (correlation coefficients  $R > 0.5$  and  $p$ -values  $P < 0.0001$ ), and have representative meso- or  
155 synoptic-scale cyclone events. The selected years were 2005 ( $R = 0.56$ ) and 2014 ( $R = 0.61$ ).



156

157 **Figure 1.** Geographic map of (a) the Southern Ocean south of 60°S, and (b) the Ross Sea. Areas in white  
158 show continental surfaces, and areas in light grey indicate the ice shelves. The color scale indicates the  
159 bathymetry. In (a), the Ross Sea model domain is shown by the red solid box, and the brown dashed box  
160 represents the area shown in (b). In (b), the magenta pentacle indicates the position of McMurdo Station,

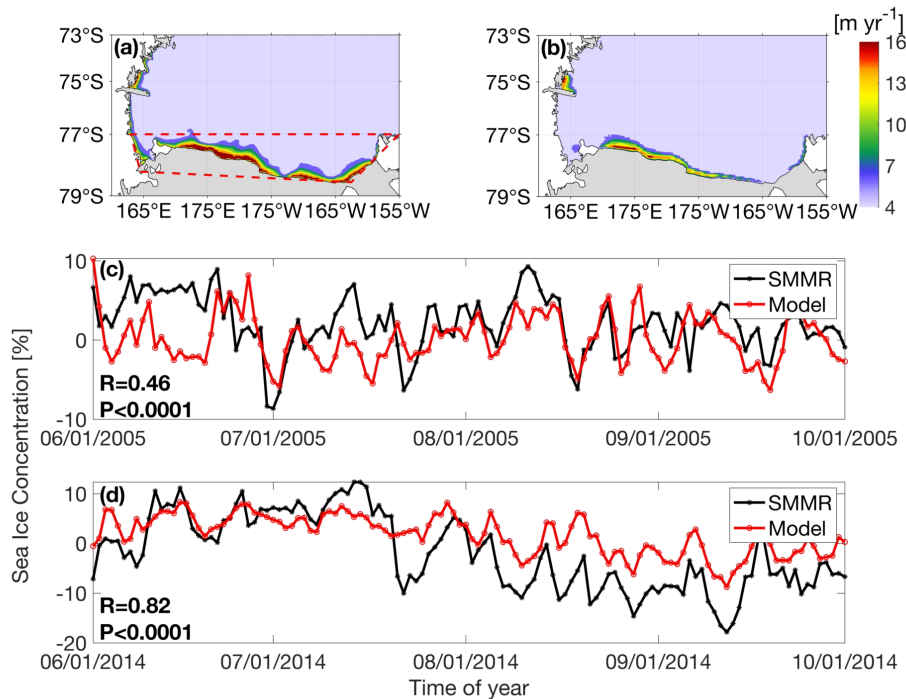


161 and the red lines indicate the S1, S2, and S3 sections crossing the troughs that are the major passages for  
162 HSSW outflows towards the slope.

163

### 164 2.3 Model validation

165 The performance of the Ross Sea model in reproducing sea ice concentration in the RISP was evaluated by  
166 comparing the annual cumulative SIP from the model simulation with the estimates from satellite data. The  
167 annual cumulative SIP averaged over 2003–2010 in the RISP presents similar spatial patterns between the  
168 simulation and observations (Figs. 2a–b). Compared with the observations, the model slightly  
169 overestimates the SIP, which is a common problem with the Southern Ocean ocean-sea-ice models used  
170 for studying Antarctic coastal polynyas (Zhang et al., 2015; Kusahara et al., 2017; Wang et al., 2021). The  
171 integrated SIP volumes over the RISP are  $6.74 \cdot 10^2$  and  $5.76 \cdot 10^2 \text{ km}^3 \text{ yr}^{-1}$  for modelled and observed datasets  
172 respectively. Such a SIP overestimation is possibly associated with the relatively coarse resolution of the  
173 atmospheric forcing fields compared to the actual wind conditions. The atmospheric model with too low  
174 resolution possibly extends orographic slopes seaward, beyond the actual coastline, and thus induces too  
175 strong offshore winds, which in turn enhance SIP in the coastal polynyas (Stössel et al., 2011). Statistical  
176 analysis of comparisons for daily SIP anomalies in winters (June–September) of 2005 and 2014 from  
177 climatological values was conducted, and the results are shown in Figs. 2c and 2d. Correlation coefficients  
178 between the modeled and observed sea ice concentration in RISP in 2005 and 2014 are 0.46 ( $P < 0.001$ ) and  
179 0.82 ( $P < 0.0001$ ), respectively (Figs. 2c–d), suggesting that the model captures the daily variability of ice  
180 concentration well.



181

182 **Figure 2.** (a–b) Annual cumulative sea ice production rates over the Ross Sea from (a) the Ross Sea model  
183 and (b) the AMSR-E product averaged over 2003–2010. The polygon in (a) enclosing the Ross Ice Shelf  
184 Polynya was used to analyse the HSSW characteristics. (c–d) Time series of observed (black lines) and



185 modelled (red lines) daily polynya-averaged sea ice concentration anomalies in June–September of 2005  
186 and 2014.

187

## 188 2.4 Analysis methods

189 The extent of RISP was defined as the area where the multi-year-average annual cumulative SIP is greater  
190 than zero based on the Ross Sea model results. The HSSW is defined as the water mass with potential  
191 density ( $\sigma_\theta$ ) above  $28 \text{ kg m}^{-3}$  (Yoon et al., 2020). Temperature-salinity (T-S) analysis was conducted over  
192 the defined RISP polygon region presented in Fig. 2a to elucidate the impacts of cyclones on the HSSW  
193 formation. The HSSW export rates were calculated across three transects (Fig. 1b) located over three  
194 troughs: the Drygalski Trough (S1), the Joides Trough (S2) and the Glomar Challenger Trough (S3) that  
195 are the major HSSW outflow passages.

196

197 Cyclones were tracked by the University of Melbourne Automatic Cyclone Tracking Scheme (Murray and  
198 Simmonds, 1991), based on the ERA-Interim reanalysis product from 1999 to 2014. The optimal  
199 parameters used in this scheme, including the horizontal air pressure field smoothing parameter, the radius  
200 used for the calculation of Laplacian pressure, and the maximum topographic height for detecting the  
201 cyclones, adopted the values by Uotila et al. (2009). The identified cyclone properties included their  
202 locations, lifetimes, and mean radii among others. Cyclones were selected according to the criteria that they  
203 should have lifetimes longer than 12 hours and the distance between their first and last detected locations  
204 should be greater than 1000 km. Such criteria are likely to exclude detected but unrealistic cyclones (Uotila  
205 et al., 2011). We divided the area south of  $42^\circ\text{S}$  into 720 sectors, each one spanning  $4^\circ$  in latitude and  $6^\circ$  in  
206 longitude, and calculated cyclone track densities, defined as the number of cyclone tracks per each sector  
207 (Uotila et al., 2013) over 1999 to 2014 (Fig. 3). The cyclones were categorized into two types depending  
208 on their horizontal scale: synoptic-scale cyclones with length scales 1000 km or longer, and mesoscale  
209 cyclones with shorter than 1000 km length scales (Heinemann, 1990; Bromwich, 1991; Carrasco et al.,  
210 2003; Uotila et al., 2011). In this study, we selected two representative synoptic-scale cyclone events that  
211 had different paths over the study region, and one mesoscale cyclone event. These three events occurred in  
212 June 2005 (labeled as MESO), July 2005 (labeled as SYNO1) and September 2014 (labeled as SYNO2).

213

214 A three-dimensional momentum analysis of ocean flow was conducted to elucidate the potential  
215 mechanisms for the HSSW export variability under the impact of a typical cyclone. Each momentum term  
216 was analyzed to diagnose the dominant term related to the export variability. The three-dimensional along-  
217 shelf and cross-shelf momentum equations are

$$218 \quad \frac{\partial u}{\partial t} = - \left( u \frac{\partial u}{\partial x} + v \frac{\partial u}{\partial y} + w \frac{\partial u}{\partial z} \right) + f v - \frac{1}{\rho_0} \frac{\partial p}{\partial x} + K_V \frac{\partial^2 u}{\partial z^2} + K_H \left( \frac{\partial^2 u}{\partial x^2} + \frac{\partial^2 u}{\partial y^2} \right) \quad (1)$$

219 and

$$220 \quad \frac{\partial v}{\partial t} = - \left( u \frac{\partial v}{\partial x} + v \frac{\partial v}{\partial y} + w \frac{\partial v}{\partial z} \right) - f u - \frac{1}{\rho_0} \frac{\partial p}{\partial y} + K_V \frac{\partial^2 v}{\partial z^2} + K_H \left( \frac{\partial^2 v}{\partial x^2} + \frac{\partial^2 v}{\partial y^2} \right), \quad (2)$$

221 respectively, where  $u$  and  $v$  are the alongshore and cross-shore components of velocity,  $f$  is the Coriolis  
222 parameter,  $\rho_0$  is the reference density of  $1025 \text{ kg m}^{-3}$ ,  $p$  is pressure,  $x$  is the along-shelf coordinate,  $y$  is the  
223 cross-shelf coordinate,  $K_V$  and  $K_H$  are the vertical and horizontal eddy viscosity coefficients respectively.  
224 Vertical momentum and tracer mixing were calculated using the K-profile parameterization (KPP; Large  
225 et al. 1994). Each term of the momentum equations was calculated for each model time step and output as  
226 6-hourly averages.

227

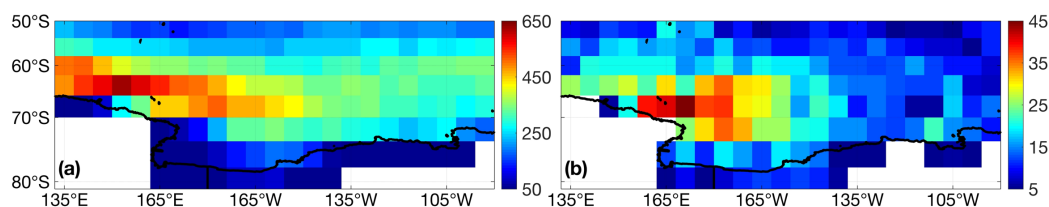


## 228 3 Results and Discussions

### 229 3.1 Cyclone track densities

230 The track density of synoptic-scale cyclones can be up to 10–14 times higher than that of mesoscale  
231 cyclones in the Ross Sea and the surrounding regions (Fig. 3). Such discrepancy between synoptic-scale  
232 and mesoscale cyclones could be related to the relatively coarse spatial resolution of the ERA-Interim  
233 product, which may not capture all smaller systems like mesoscale cyclones (Condrón et al., 2006; Uotila  
234 et al., 2009; Uotila et al., 2011). However, the spatial distributions of cyclones revealed in this study are  
235 consistent with the features in Uotila et al. (2011), which are derived from the AMPS high-resolution dataset.  
236 The high track density of synoptic-scale cyclones extends to the continental shelf and coastal regions in the  
237 western Ross Sea (Fig. 3a). For mesoscale cyclones, a large number of track densities appear at the center  
238 of the Ross Sea (at about 180° meridional) in front of the RIS central region (Fig. 3b), which may be related  
239 to the cold air outbreaks from the continental interior (Seefeldt and Cassano, 2008; Turner et al., 2009). For  
240 synoptic-scale cyclones, two events were selected for our study, which occurred in July 2005 and  
241 September 2014, respectively. The first event originated in the area north of the central Ross Sea, and then  
242 moved south-eastwards before finally reaching the eastern coastal region. The path of the cyclone related  
243 to this event was located in the area with high track densities shown in Fig. 3a. The onset and development  
244 of the second cyclone in September 2014 event were primarily situated along the northeastern part of the  
245 Ross Sea (about 130°W), accompanied by a slight east-west movement. Although the latter event has a  
246 different trajectory than the earlier one, it was also located in the high track-density area (Fig. 3a). For the  
247 mesoscale system, we chose one representative event occurring in June 2005. This cyclone moved  
248 southeastward from the north-western continental shelf region and lingered in the central Ross Sea, where  
249 the track density is higher compared to nearby areas (Fig. 3b).

250



251

252 **Figure 3.** (a–b) Accumulated track densities (the number of tracks per section) of (a) synoptic-scale  
253 cyclones and (b) mesoscale cyclones in the Ross Sea and surrounding regions over 1999–2014.

254

### 255 3.2 Synoptic-scale cyclones

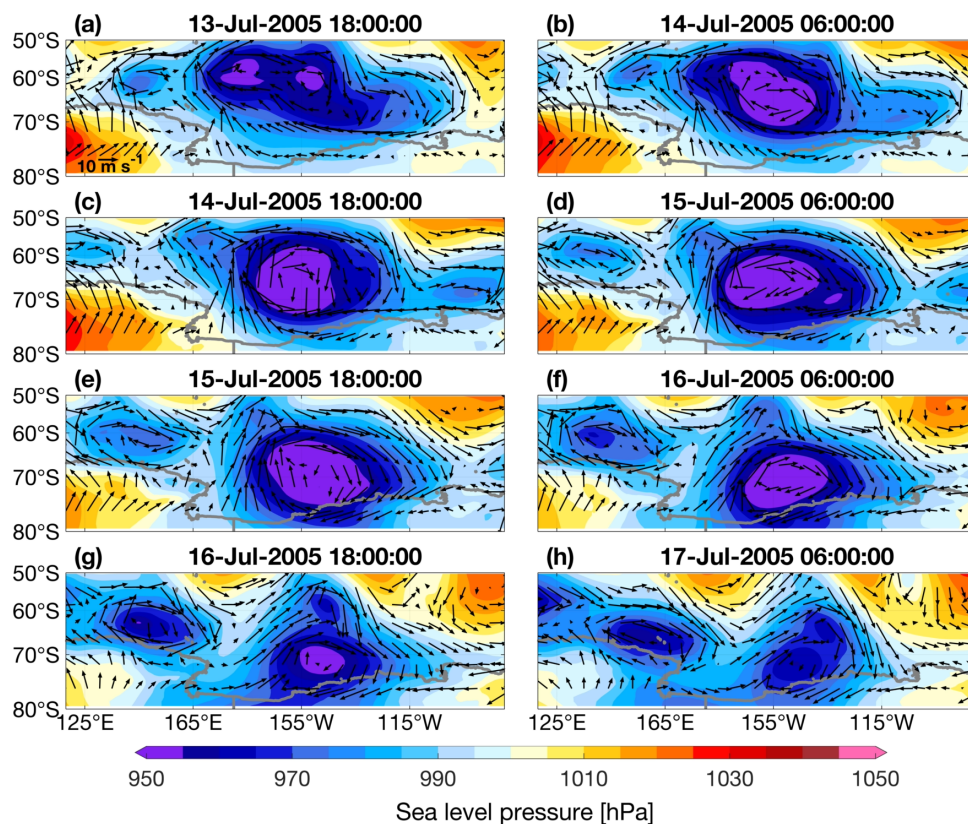
#### 256 3.2.1 The SYNO1 case

257 As mentioned in Sections 2.4 and 3.1, two representative synoptic-scale cyclones were selected over the  
258 Ross Sea region in the freezing season of 2005 and 2014 respectively. The SYNO1 occurred from July 13  
259 to July 17 of 2005. The center of this cyclone was located northeast of the Ross Sea with a diameter of  
260 about 2000 km (Fig. 4). The cyclone developed from 18:00 of July 13 to 06:00 of July 16 (Figs. 4a–f), and  
261 in this time period there was a dramatic increase in the offshore wind over the entire RIS, which was  
262 associated with the western branch of the cyclone. Corresponding to the wind change, the SIP values  
263 increased from 0.1 to 0.3 m day<sup>-1</sup> (Figs. 5a–f). Following the reduction of wind speed as the cyclone  
264 weakened and moved slightly east at 18:00 of July 16 (Fig. 4g), SIP decreased quickly to ~0.2 m day<sup>-1</sup> over  
265 the west side of RIS and ~0.1 m day<sup>-1</sup> over the east side (Fig. 5g). The coastal winds turned onshore at



266 06:00 of July 17 when the cyclone weakened (Fig. 4h), and SIP decreased further (Fig. 5h), indicating near-  
267 instantaneous response of sea ice formation to the wind changes. The differences in the meridional wind speed  
268 speed and SIP between the normal and cyclone conditions averaged over the RISIP are summarized in Table  
269 1. For SYNO1, the wind speed was about 1.4 times larger than the normal values, i.e. from 4.8 to 6.5 m s<sup>-1</sup>,  
270 while polynya-averaged SIP increased by 23% reaching 0.043 m day<sup>-1</sup>.

271

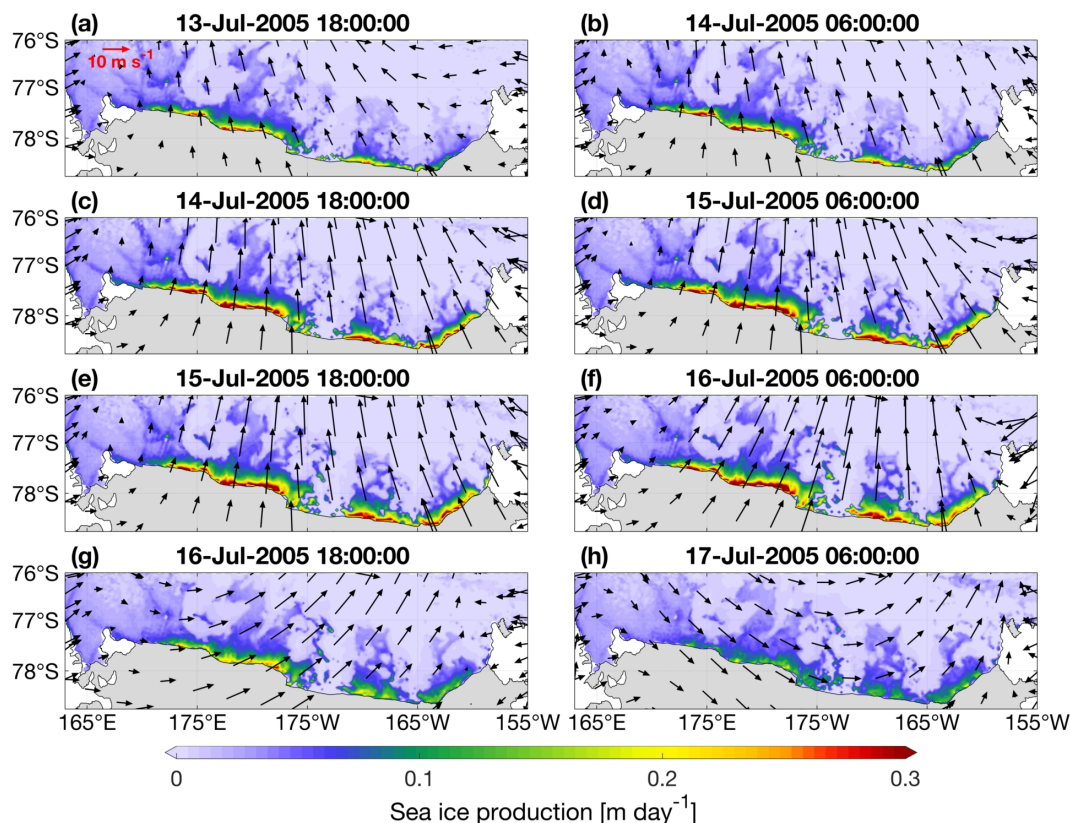


272

273 **Figure 4.** (a–h) Spatial distributions of 12-hour-average sea level pressure (color shading) and 10-m wind  
274 vectors (black arrows) in the Ross Sea and surrounding regions over 13–17 July 2005.

275





276

277 **Figure 5.** (a–h) Spatial distributions of 12-hour-average wind vectors and sea ice production (color shading)  
 278 in the Ross Ice Shelf Polynya over 13–17 July 2005.

279

280 **Table 1.** Comparisons of polynya-averaged sea ice production rates and HSSW properties under the normal  
 281 and selected synoptic- and meso-scale cyclones (SYNO1, SYNO2 and MESO) for the RISP. The normal  
 282 values are calculated prior to these events, from 06:00 of July 13 to 18:00 of July 13 for SYNO1, 12:00 of  
 283 September 16 to 00:00 of September 18 for SYNO2 and 18:00 of June 20 to 12:00 of June 21 for MESO.  
 284 The cyclone time ranges used in the calculation are consistent with those shown in Figs 4, 8 and 11.

Properties	SYNO1		SYNO2		MESO		
	Normal	Cyclone	Normal	Cyclone	Normal	Cyclone	
Meridional wind speed ( $\text{m s}^{-1}$ )	4.8	6.5	2.8	5.2	-3.3 <sup>a</sup>	7.1 <sup>a</sup>	
Sea ice production ( $\text{m day}^{-1}$ )	0.035	0.043	0.029	0.037	0.026 <sup>a</sup>	0.045 <sup>a</sup>	
HSSW volume ( $10^4 \text{ km}^3$ ) <sup>b</sup>	3.18	3.22	3.54	3.59	2.96	2.97	
HSSW export (Sv)	S1	-1.16	-1.12	1.06	0.58	-0.35	-0.55
	S2	0.22	-0.85	0.51	-0.44	0.35	0.65
	S3	2.01	1.05	0.79	1.25	-0.06	1.63

285

<sup>a</sup>The calculation was conducted for the region west of 175°W within the defined RISP, as the eastern region  
 286 is dominated by onshore winds, resulting in no significant change in SIP.

287

<sup>b</sup>The calculation was performed with a 24-hour lag for synoptic-scale events and a 12-hour lag for  
 288 mesoscale event respectively, based on the discovered lag time of HSSW volume response to the cyclones.



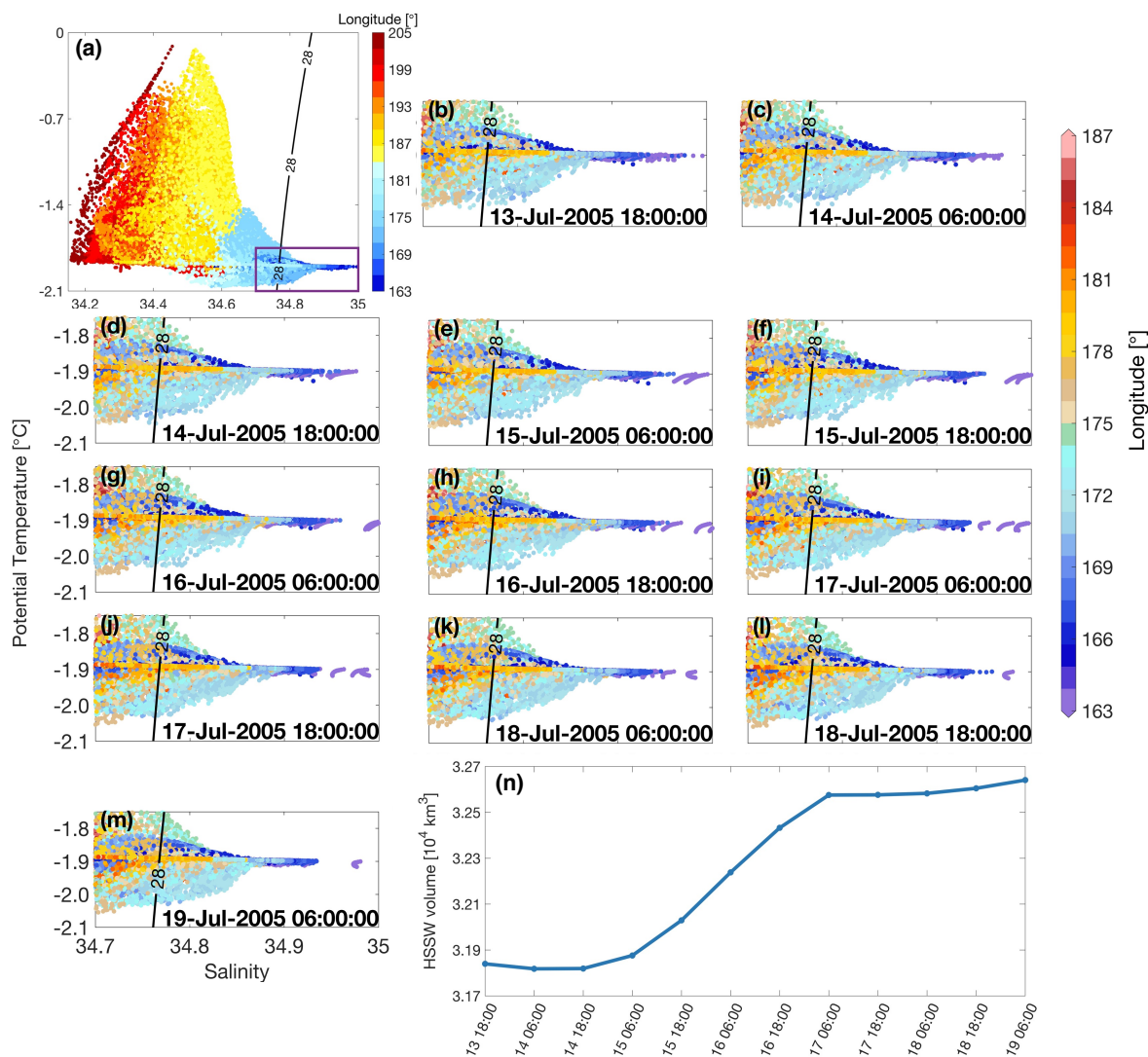
289

290 The water mass properties and HSSW volume in the RISP region during the SYNO1 event are illustrated  
291 in Fig. 6. Note that HSSW was mainly formed in the western section of RISP (163°E–175°E) and fresher  
292 water accumulated from 175°E to 155°W (Fig. 6a), which is consistent with previous studies that observed  
293 the highest HSSW accumulation in the western sector of the Ross Sea (Jacobs et al., 1985; Budillion et al.,  
294 2003 ; Mathiot et al., 2012). The amount of HSSW with higher salinity (34.95–35 psu) increased over the  
295 western coastal region in 163°E–164°E from 18:00 of July 14 to 06:00 of July 16 (Figs. 6d–g), when a  
296 dramatic increase in SIP occurred in this area accompanied by the intensification of the SYNO1 cyclone.  
297 The HSSW salinity reached about 35 psu at 06:00 of July 15 (Fig. 6e) when the cyclone had intensified for  
298 2 days. The increase in the higher-salinity HSSW amount persisted for 2 days after the decay of the cyclone  
299 (Figs. 6h–k), and then the amount started decreasing (Figs. 6l–m). The HSSW volume in the RISP area  
300 kept increasing when SYNO1 intensified from 18:00 of July 14 to 06:00 of July 16 and reached the  
301 maximum at 06:00 of July 17 (Fig. 6n), so the HSSW formation could persist at least 1 day after the cyclone  
302 weakened. For the SYNO1 event, the HSSW volume increased by  $0.04 \cdot 10^4 \text{ km}^3$  compared to the value  
303 before the cyclone.

304

305 The HSSW exports across the three selected transects (S1, S2 and S3 in Fig. 1b) were calculated and related  
306 to the changes in meridional winds (Figs. 7a, b). The northward winds increased slightly from 18:00 of July  
307 13 to 18:00 of July 14 and then turned onshore at 06:00 of July 17 (Figs. 7a, b), associated with the evolution  
308 of the SYNO1 cyclone. The export of HSSW across S1 has a significant negative correlation with the  
309 meridional wind speed ( $R=-0.70$ ,  $P=0.012$ ), suggesting that the HSSW had stronger eastward (negative)  
310 transport across the meridionally directed transect S1 when the wind speed increased. The transport across  
311 the zonally directed transect S3 significantly and positively correlated with the meridional wind speed  
312 ( $R=0.75$ ,  $P=0.005$ ). The averaged current velocity on S1 and S3 both have strong positive correlations with  
313 HSSW export ( $R>0.98$  and  $P<0.0001$ , not shown), suggesting that the velocity is the dominant factor  
314 regulating the export (Figs. 7a, b). Time series of HSSW export and wind speed for Transect S2 are not  
315 shown as no significant correlation between these two variables was detected. The vertical sections of  
316 potential density and circulation along the transects S1–S3 were analyzed to identify physical mechanisms  
317 behind the correlations discussed above (Figs. 7c–n). When the offshore wind speed decreased between 14  
318 and 17 July (Fig. 7a), there was no significant change in the distribution of HSSW along S1 (Figs. 7f, i and  
319 l). Meanwhile, there was notable change in the cross-transect current velocity: the negative (eastward)  
320 velocity in the upper layer between 76.7°S and 76.5°S decreased significantly, while the positive (westward)  
321 velocity in the bottom layer increased (Figs. 7f to i and l). Both features could lead to enhanced exports  
322 when the wind speed decreased. When the offshore wind speed increased between 06:00 and 18:00 of July  
323 13 (Fig. 7a), changes in the cross-transect current velocity on S1 were exactly the opposite of those found  
324 during the decrease of the wind (Figs. 7c to f). For S3, the distribution of HSSW had a slight change, while  
325 the change in velocity is much more pronounced between 178.4°E and 178.7°W, where the positive  
326 (northward) velocity decreased on the west side and the negative (southward) velocity increased on the east  
327 side (Figs. 7h, k and n) when the offshore wind speed decreased (Fig. 7b), resulting in a decrease in HSSW  
328 export which is positively correlated with the wind speed. The dynamical mechanisms for the change in  
329 currents will be discussed in Section 3.4. For S2, although there is no significant correlation between the  
330 HSSW export and the wind speed, the vertical distribution shows a decrease in northward export (Figs. 7d,  
331 g, j and m).

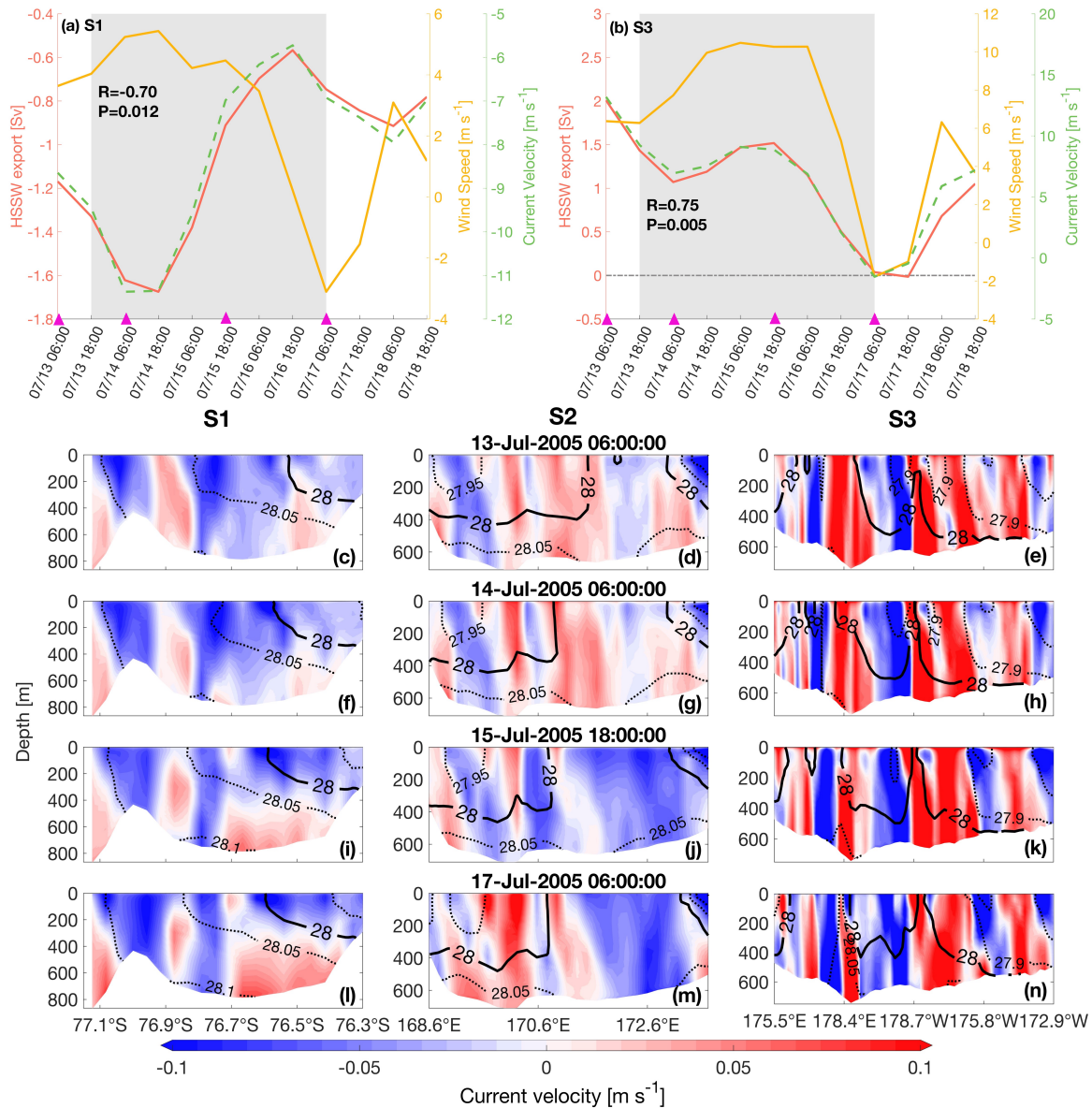
332



333

334 **Figure 6.** (a–m) Temperature–salinity (T–S) diagrams for the RISP region shown in Fig. 2a. The T–S dots  
 335 are color-coded with longitude. The black isline denotes the potential density contour of 28 kg m<sup>-3</sup>. (a) T–  
 336 S diagram covering the entire salinity range at 18:00 on July 13, 2005. (b–m) T–S diagrams are bounded  
 337 by the purple box shown in (a) and represent values during the SYNO1 event from July 13 to July 19 of  
 338 2005. (n) Time series of HSSW volume over the RISP from 18:00 of July 13 to 06:00 of July 19 2005.

339



340

341 **Figure 7.** (a) Time series of averaged meridional winds along the S1 transect (see Fig. 1), HSSW exports  
 342 across the S1 and averaged current velocity along the S1 from 06:00 of July 13 to 18:00 of July 18 2005.  
 343 The gray shading represents the time of the SYNO1 event. The correlation coefficient  $R$  and  $P$ -value were  
 344 calculated between the HSSW export and meridional winds. (b) Same as Fig. 7a but for S3. (c–n) Vertical  
 345 sections of cross-transect current velocity (color shading) and potential density (contour lines) on (c, f, i  
 346 and l) S1, (d, g, j and m) S2 and (e, h, k and n) S3 at four selected time moments (indicated by the magenta  
 347 triangles in (a) and (b)). Positive values denote currents from the RISP toward the open ocean, i.e. westward  
 348 for S1 and northward for S2 and S3. The bold black contour line indicates the isopycnal of  $28 kg m^{-3}$ .

349

350



### 351 3.2.2 The SYNO2 case

352 The second selected synoptic-scale cyclone (SYNO2) developed from 00:00 of September 18 to 12:00 of  
353 September 22 2014, and was located on the eastern side of the Ross Sea close to the Amundsen Sea, which  
354 is further east than the SYNO1 event (Fig. S1). The entire period of this synoptic-scale cyclone can be  
355 divided into three stages. In Stage I, the cyclone developed and the low-pressure center expanded in all  
356 directions (Figs. S1a–d). In Stage II, the center moved eastward (Figs. S1e–g). In Stage III, the cyclone  
357 rapidly decayed (Figs. S1h–j). The spatial pattern of SIP in the RISP is displayed in Fig. S2. During Stage  
358 I, SIP increased over the entire RISP due to the strong offshore winds (Figs. S2a–d), and the increase was  
359 more pronounced on the western side of the polynya compared to the eastern side. As the cyclone entered  
360 stage II, SIP showed the opposite changes over the eastern and western sides compared to Stage I, when  
361 the offshore wind over the western polynya was still strong but the wind over the eastern polynya had  
362 significantly turned and weakened (Figs. S2e–g). There was a notable SIP decrease over the entire RISP  
363 when the SYNO2 cyclone decayed in Stage III (Figs. S2h–j). Similar to SYNO1, SIP quickly responded to  
364 the variation of winds over the entire RISP. For the SYNO2 event, the area-averaged wind speed increased  
365 by almost 2 times than before cyclone's arrival, reaching  $5.2 \text{ m s}^{-1}$ . The area-averaged SIP showed an  
366 increase of about 28%, reaching  $0.037 \text{ m day}^{-1}$  (Table 1).

367

368 For the water mass response, HSSW volume in the RISP increased significantly until 00:00 on 22  
369 September and then remained at  $3.62 \cdot 10^4 \text{ km}^3$  for at least 60 hours (Fig. S3a). The salinity of newly formed  
370 HSSW increased to 35.1 psu during Stage I of the SYNO2 cyclone (Figs. S3b–e), but slightly decreased at  
371 00:00 of September 20 (Fig. S3f), possibly associated with the decreased SIP at the eastern side of RISP  
372 (Fig. S2e). Afterwards, the formation of higher-salinity HSSW kept increasing near  $163^\circ\text{E}$  for 36 hours  
373 when the coastal SIP was already decreasing (Figs. S2 and S3k–m). Therefore, both events (SYNO1 and  
374 SYNO2) revealed persistent impacts of cyclones on the HSSW formation over the western RISP, even after  
375 these weather systems had decayed. The HSSW exports across the three transects (S1–S3) were calculated  
376 during the SYNO2 event but are not shown as the meridional winds and the HSSW exports across S1 and  
377 S2 did not correlate. For S3 on the other hand, there was a positive significant correlation between the  
378 meridional wind speed and the HSSW export 12-hours later ( $R=0.51$ ,  $P=0.055$ ). As shown in Table 1, there  
379 was an increase in the HSSW volume during SYNO2, being  $0.05 \cdot 10^4 \text{ km}^3$  larger than the rate before the  
380 event. The HSSW export across S3 increased about 58% when the wind speed increased from 2.8 to  $5.2 \text{ m s}^{-1}$ ,  
381 while the export across S1 and S2 decreased.

382

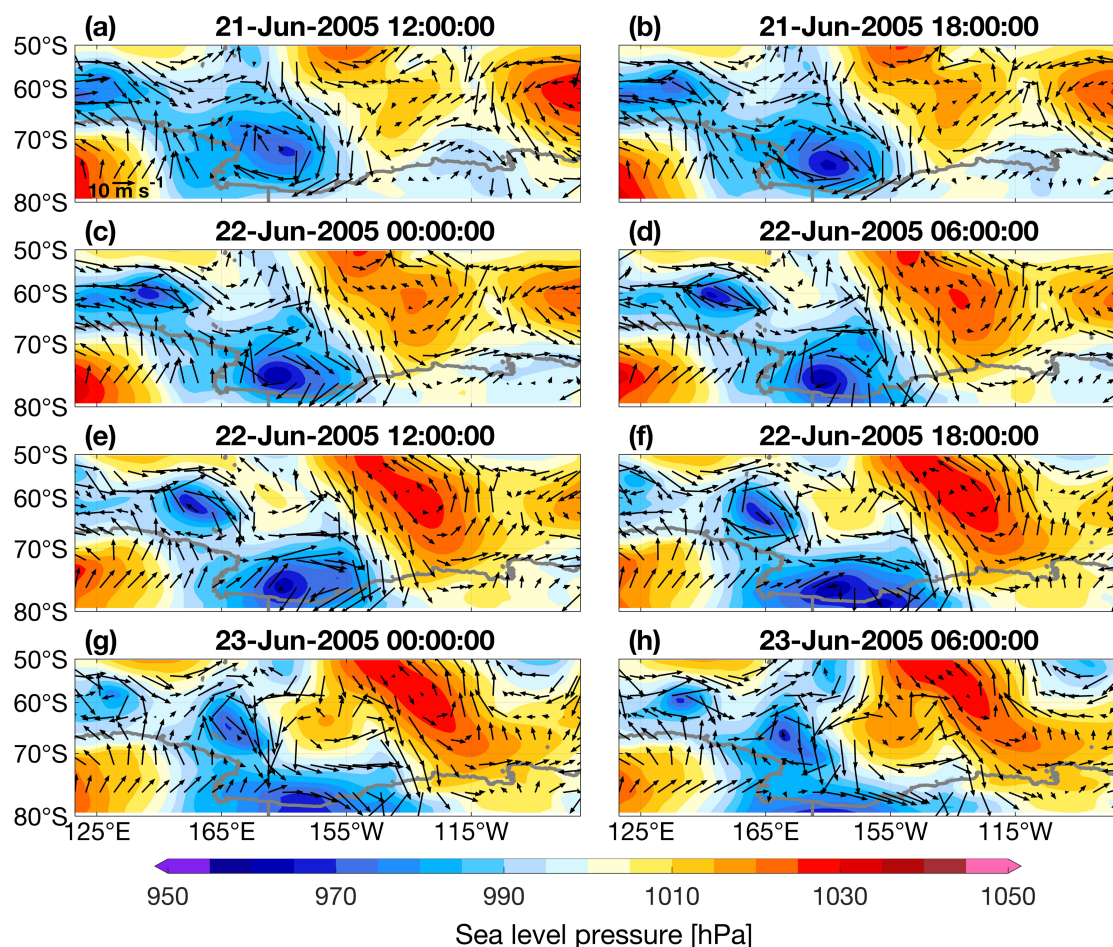
### 383 3.3 The MESO case

384 The selected mesoscale cyclone event was present around RISP from 12:00 of June 21 to 06:00 of June 23,  
385 2005, which is associated with the synoptic cyclone located farther northwest of the Ross Sea (not shown).  
386 The formation of this MESO case is consistent with earlier studies, that demonstrate the small synoptic  
387 systems could merge into mesoscale cyclones (Carrasco and Bromwich, 1993; Uotila et al., 2009). From  
388 the patterns of sea level pressure and wind vectors (Fig. 8), the center of the cyclone was located in the  
389 middle of the Ross Sea (Figs. 8c–f), and the horizontal length scale ranged from 500–1000 km. The  
390 trajectory of this cyclone was located in the area of high track densities of the Ross Sea (Fig. 3b), suggesting  
391 that it is a typical mesoscale cyclone for this region. An enlargement of the wind field is shown in Fig. 9  
392 on top of the SIP field. During the initial stage of MESO (Figs. 9a, b), the entire RISP was influenced by  
393 the southern branch of the cyclone and the prevailing alongshore wind. There was little variation in SIP, as  
394 the offshore component of wind did not significantly change. As the center of the cyclone moved south and  
395 approached RIS (Figs. 8c–e), the western and eastern sections of RISP were respectively affected by the  
396 southerly and northerly winds induced by MESO. As a result of the enhanced offshore winds, SIP in the  
397 western section increased rapidly to over  $0.3 \text{ m day}^{-1}$  (Figs. 9c–e). When the cyclone center moved further



398 south onto the ice shelf and the cyclone winds weakened (Figs. 8f–h), there was a notable decrease of SIP,  
399 suggesting that SIP responds quickly to the winds (Figs. 9f–h). In contrast to the western polynya, SIP in  
400 the eastern polynya presented a slight decrease during MESO (Figs. 9a–e), which was due to the onshore  
401 winds generated by MESO that shrunk the polynya. The response of SIP in RISP was instantaneous during  
402 these selected cyclones, which is consistent with the variation for SIP during typical strong wind events in  
403 East Antarctic coastal polynyas including the Prydz Bay and Shackleton polynyas (Wang et al., 2021).  
404 During MESO, area-averaged SIP increased by 73% than before the cyclone’s arrival (Table 1), reaching  
405  $0.045 \text{ m day}^{-1}$ , while the meridional wind speed rose from  $-3.3$  to  $7.1 \text{ m s}^{-1}$ . Thompson et al. (2020) proposed  
406 that the intensity of ice production could rise up to  $1.1 \text{ m day}^{-1}$  during the windiest events in TNB, which  
407 was calculated from the salt budget using conductivity–temperature–depth (CTD) profiles. Meanwhile, the  
408 maximum SIP rate in the RISP during MESO was  $1.2 \text{ m day}^{-1}$  in our study, which is just slightly different  
409 from the value in TNB. Differences in topography and location between the RISP and TNB could lead to  
410 such slight differences in atmospheric and hydrological conditions.

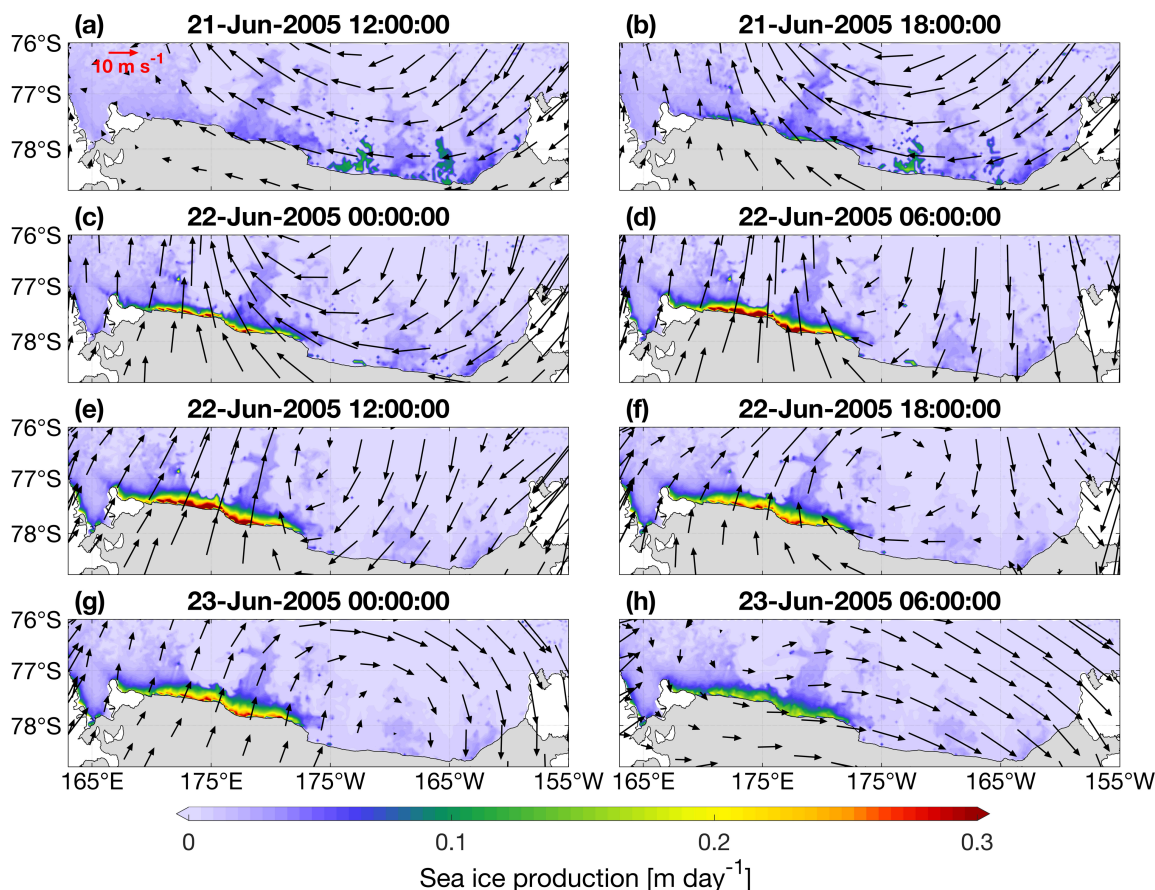
411



412

413 **Figure 8.** (a–h) Spatial distributions of 6-hour-average sea level pressure (color shading) and 10-m wind  
414 vectors (black arrow) in the Ross Sea and surrounding regions over 21–23 June 2005.

415



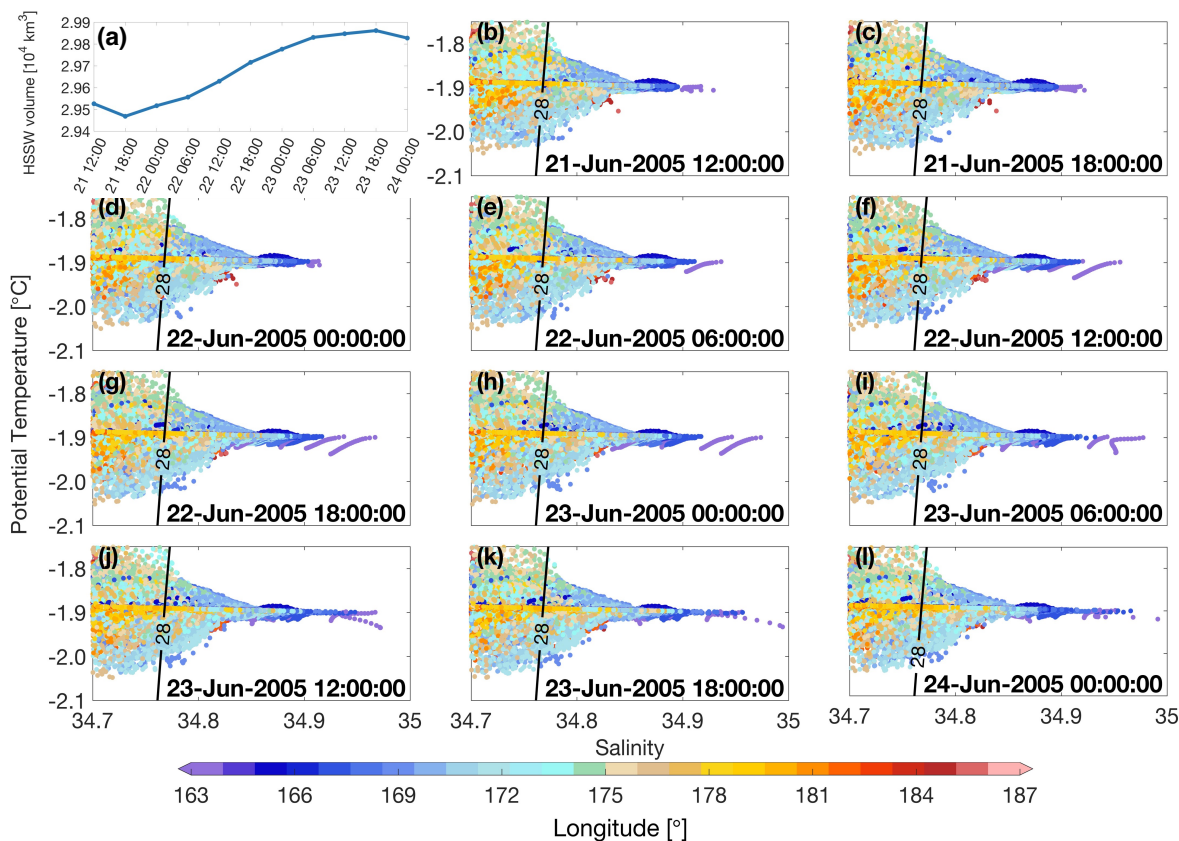
416

417 **Figure 9.** (a–h) Spatial distributions of 6-hour-average wind vectors and sea ice production (color shading)  
418 near the Ross Ice Shelf Polynya over 21–23 June 2005.

419

420 Figure 10a represents a continuous increase for HSSW volume over MESO until 18:00 on June 23 when  
421 the cyclone already disappeared. Furthermore, it can be seen from the T-S diagram of Fig. 10 that HSSW  
422 with salinity above 34.9 psu began accumulating on early June 22 (Fig. 10e), responding to the increase in  
423 SIP (Fig. 9d). The volume and salinity of HSSW increased persistently (especially in the area of 163–166°E)  
424 even during the cyclone decay when SIP was already decreasing from late June 22–23 (Figs. 9e–h and 10a,  
425 f–k). A notable feature is that the HSSW salinity was continuously in the range of 34.9–34.95 psu from  
426 12:00 to 18:00 of June 23 (Figs. 10j–k), which could be associated with a strong convection or other mixing  
427 processes. Afterwards, there was a decrease in the HSSW salinity at 00:00 am of June 24 (Fig. 10l), after  
428 about 18 hours of the departure of MESO. These features suggest that the response of the HSSW formation  
429 to a mesoscale cyclone could persist for 12–18 hours, which is a comparable time scale to synoptic cyclone  
430 events, but with a shorter time lag. The mean HSSW volume during MESO increased slightly by  $0.01 \cdot 10^4$   
431  $\text{km}^3$  compared to the volume before it. This is much smaller than changes under the synoptic cyclones  
432 SYNO1 and SYNO2 (Table 1). This difference is likely related to different spatial scales of cyclones.  
433 During MESO, only the western part of RISP was dominated by offshore winds due to the smaller spatial  
434 extent of the mesoscale cyclone, which resulted in a smaller region for HSSW production than that under  
435 synoptic-scale cyclones during SYNO1 and SYNO2.

436

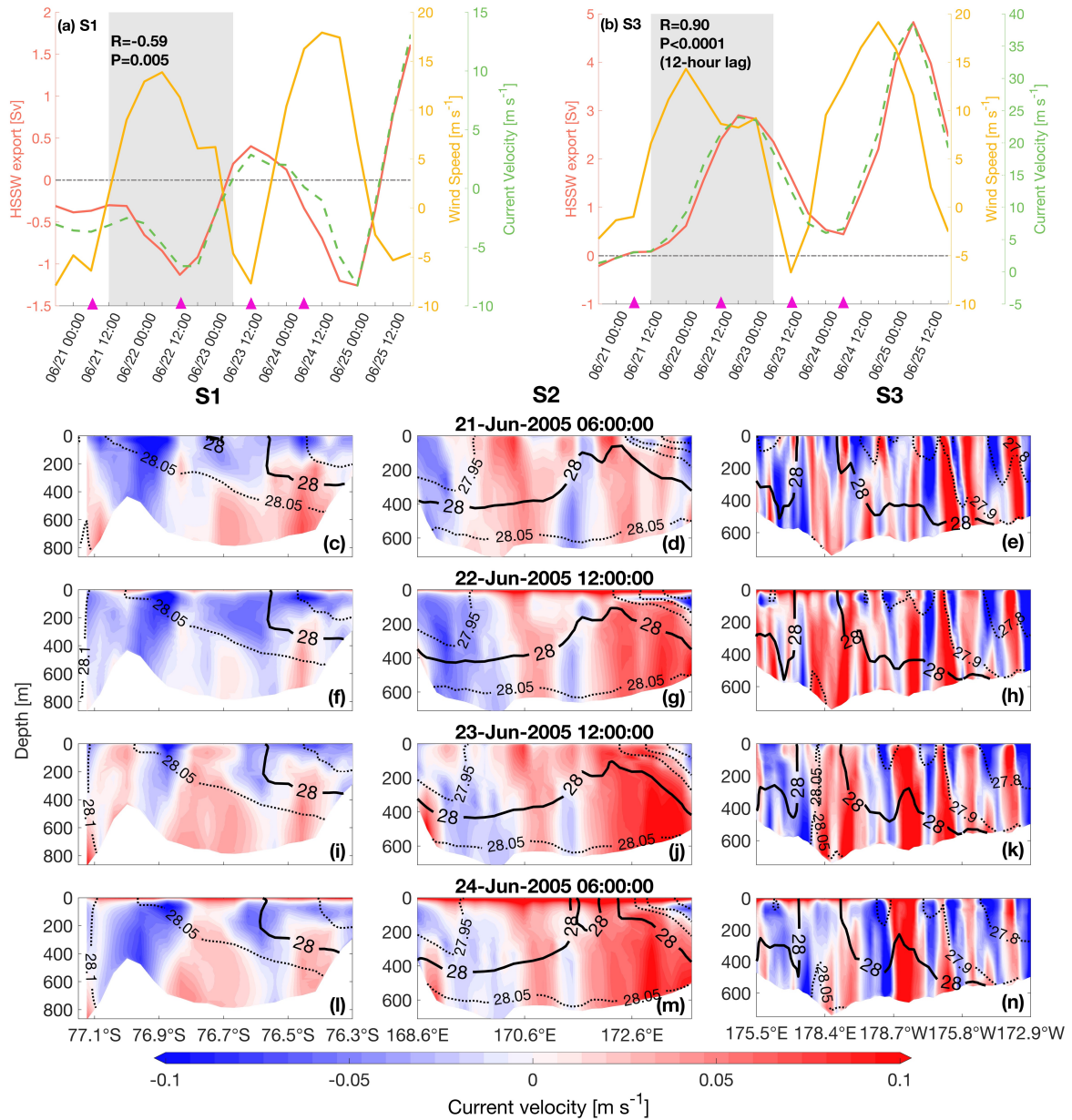


437

438 **Figure 10.** (a) Time series of HSSW volume over the RISIP from 12:00 of June 21 to 00:00 of June 24 2005.  
439 (b–l) Temperature–salinity (T–S) diagrams for the RISIP region shown in Fig. 2a. The T–S dots are color-  
440 coded with longitude. The black isoline denotes the potential density contour of  $28 \text{ kg m}^{-3}$ . T–S diagrams  
441 are bounded by the purple box shown in Fig. 6a and represent values during the MESO event from June  
442 21–24 of 2005.

443





444

445 **Figure 11.** (a) Time series of averaged meridional winds along the S1 transect (see Fig. 1), HSSW exports  
 446 across the S1 and averaged current velocity along the S1 from 18:00 of June 20 to 18:00 of June 25 2005.  
 447 The gray shading represents the time of the MESO event. The correlation coefficient  $R$  and  $P$ -value were  
 448 calculated between the HSSW export and meridional winds. (b) Same as Fig. 11a but for S3. (c–n) Vertical  
 449 sections of cross-transect current velocity (color shading) and potential density (contour lines) on (c, f, i  
 450 and l) S1, (d, g, j and m) S2 and (e, h, k and n) S3 at four selected time moments (indicated by the magenta  
 451 triangles in (a) and (b)). Positive values denote currents from the RISP toward the open ocean, i.e. westward  
 452 for S1 and northward for S2 and S3. The bold black contour line indicates the isopycnal of  $28 \text{ kg m}^{-3}$ .

453



454 The HSSW exports across the transects S1–S3 over the period of the mesoscale cyclone MESO are shown  
455 in Fig. 11. To better investigate the relationship between the HSSW export and the cyclone event,  
456 distributions of wind vectors and sea level pressure were examined for about two days after the end of  
457 MESO (i.e. until June 25). The two maxima of wind speed time series are associated with two consecutive  
458 mesoscale cyclones (Figs. 11a–b). For Transect S1, there is a significant, non-lagged negative correlation  
459 between the meridional wind speed and HSSW export from June 21 to June 25 ( $R=-0.59$ ,  $P=0.005$ ) (Fig.  
460 11a). However, relationships of wind speed and HSSW export across S1 and S3 are different. The HSSW  
461 export across S3 is significantly and positively related to the wind speed with a 12-hour lag ( $R=0.90$ ,  
462  $P<0.0001$ ). The export across S2 has a negative correlation with wind speed, though weaker compared to  
463 S1 ( $R=-0.44$  and  $P=0.05$ , not shown). For transects S1 and S3, the current velocity is significantly and  
464 positively correlated with the HSSW export with no lag ( $R>0.96$  and  $P<0.0001$ , Figs. 11a–b), resembling  
465 the SYNO1 case. As there is a 12-hour lag correlation between wind speed and current velocity for S1,  
466 such a relationship can explain why the HSSW export also exhibited a 12-hour-lag response to the wind  
467 speed for S1. The HSSW export decreased by 57% across S1 and increased by 1.69 Sv across S3 when the  
468 offshore wind speed increased from  $-3.3$  to  $7.1$   $\text{m s}^{-1}$  compared to the values before MESO (Table 1).  
469 Vertical sections for ocean currents and potential density are presented in Figs. 11c–n. For S1, positive  
470 (westward) transports were observed in the upper 50 m (Figs. 11f and l) when offshore wind speed became  
471 stronger, which can be interpreted as enhanced westward Ekman transport (Fig. 11a). Consistent with the  
472 features found under synoptic-scale cyclones, the major factor inducing the change in HSSW export across  
473 S1 is the current velocity change below 50 m: the westward velocity increased between  $77.1$ – $76.9^\circ\text{S}$  and  
474  $76.7$ – $76.5^\circ\text{S}$  corresponding to the increase of wind speed, and the eastward velocity decreased in the central  
475 section between  $76.9$ – $76.7^\circ\text{S}$  (Figs. 11c to f and i to l), ultimately leading to a negative correlation between  
476 the wind speed and the HSSW export. For S2, the most eminent feature is that the export of HSSW is  
477 mainly concentrated on the eastern side of the section (Figs. 11d, g, j and m). For S3, there was no  
478 significant change in HSSW compared to the change in current velocity. The sharp change in current  
479 velocity around  $178.4^\circ\text{E}$  dominates the variation of HSSW export (Figs. 11e, h, k and n).

480

### 481 3.4 Potential mechanisms for the HSSW export variations

482 As illustrated in Section 3, for both SYNO1 and MESO, the HSSW export across S1 was negatively  
483 correlated with the meridional wind speed, while export across S3 was positively correlated (Figs. 7a–b  
484 and Figs. 11a–b). These relationships also exist over the longer time periods of June–September in 2005  
485 and 2014 but with relatively lower correlation coefficients ( $R=-0.27$ ,  $P<0.0001$  with a lag of 6–12 hours for  
486 S1 and  $R=0.42$ ,  $P<0.0001$  with a 12-hour lag for S3). Meanwhile, it is clear that the current velocity is the  
487 dominant factor in modulating the HSSW export change compared to the HSSW volume for both S1 and  
488 S3 (Figs. 7 and 11). Then, to elucidate the dynamical control for the current variations, we examined the  
489 momentum budgets for S1 and S3 in SYNO1 and MESO. For SYNO1, the momentum balance presents  
490 similar results to those of MESO and is not shown. The vertical sections of momentum terms on S1 and S3  
491 in MESO are displayed in the cross-shelf (Fig. 12) and along-shelf (Fig. 13) directions respectively. For  
492 both directions, the momentum budgets were dominated by the Coriolis acceleration and pressure gradient  
493 terms, and the other terms were an order of magnitude smaller (Figs. 12 and 13). As such, the flows across  
494 these transects (in the along-shelf direction for S1 and the cross-shelf direction for S3) were primarily  
495 geostrophic (Figs. 12 and 13).

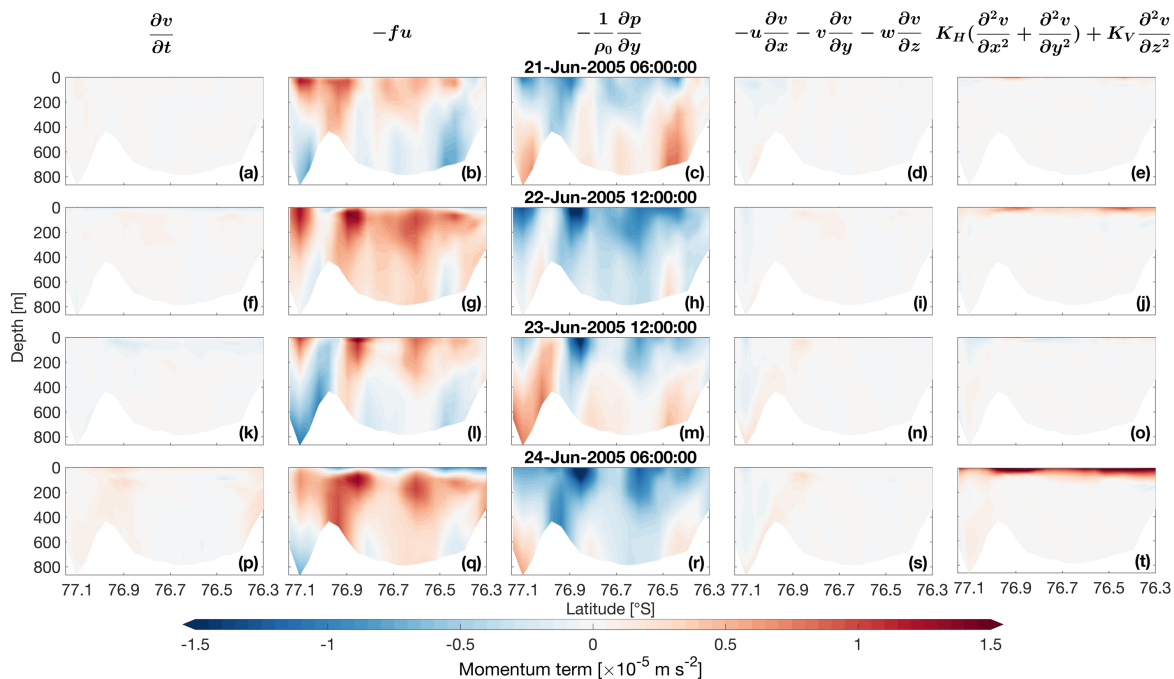
496

497 For S1, there were two zones ( $77.1$ – $76.9^\circ\text{S}$  and  $76.7$ – $76.5^\circ\text{S}$ ) where the current velocity changed notably  
498 (Figs. 11c, f, i and l) during MESO, corresponding to the change in the Coriolis (Figs. 12b, g, l and q) term,  
499 which was associated with the change in the pressure gradient (Figs. 12c, h, m and r) term. We then  
500 examined the spatial distribution of sea surface elevation over the Ross Sea (Fig. 14), where negative values



501 near the RIS close to S1 existed persistently. Such distribution resulted in southward (negative) pressure  
 502 gradient force due to sea surface differences over S1, leading to an eastward geostrophic flow across S1.  
 503 When the wind speed increased at 12:00 of June 22 and 06:00 of June 24 (Fig. 11a), the pressure gradient  
 504 force was larger than that under lower wind speeds (compare Figs. 14b and 14d to 14a and 14c). These  
 505 features suggest that the increased offshore winds induced intensified westward Ekman transports in the  
 506 upper layer over 74–76.5°S and 163–173°E just north of S1 (Fig. S4), eventually resulting in the higher sea  
 507 surface in this region (Figs. 14b and 14d). Meanwhile, the relatively strong vertical shear in the upper layer  
 508 suggests that the Ekman transport could dominate on top of the interior geostrophic current (Figs. 12j and  
 509 12t). However, near the RIS over 163–173°E where offshore winds also prevailed, the increase in surface  
 510 elevation could barely be detected. After examining the horizontal pattern of currents over the Ross Sea,  
 511 we found a current flowing from west to east across S1 located north of the Ross Island, which further  
 512 flowed southward below the RIS (Fig. S4) in the upper layer. Previous studies showed that there is an  
 513 HSSW inflow underneath the RIS through the Ross Island (Budillon et al. 2003), which could advect more  
 514 than 10% of HSSW to the southern part of RIS, and intensify continuously over the winter (Jendersie et al.  
 515 2018). Therefore, we speculate this southward inflow as one of the reasons for the persistent low sea surface  
 516 elevation in the area close to the RIS (Fig. 14).

517



518

519 **Figure 12.** (a–t) Vertical sections of the momentum equation terms (Eq. (2)) along S1 at four selected time  
 520 moments during the MESO event (indicated by the magenta triangles in Figs. 11a and 11b): (a, f, k and p)  
 521 local acceleration, (b, g, l and q) Coriolis acceleration, (c, h, m and r) pressure gradient, (d, i, n and s)  
 522 nonlinear advection and (e, j, o and t) eddy viscosity in the cross-shelf momentum budget.

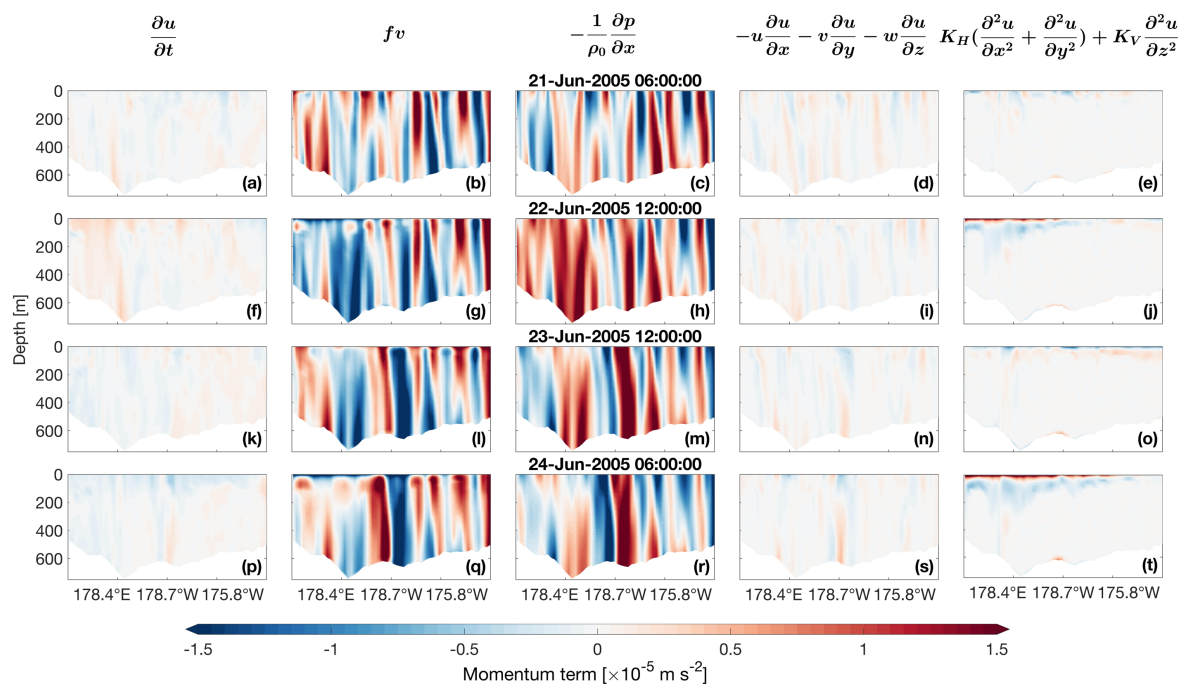
523

524 Along S3, the western section (around 178.4°E) with a considerable velocity change (Figs. 11e, h, k and n)  
 525 dominated the variation of HSSW export. Meanwhile, an outward (northward) flow can be seen clearly  
 526 over the Glomar Challenger Trough across the western section (marked by the red box in Fig. S4). From  
 527 the distribution of sea surface elevation, it is noted that the elevation was lower when the wind speed



528 increased over the Glomar Challenger Trough (Figs. 14b and 14d), which might be associated with the  
 529 divergent Ekman transports caused by the cyclone. Such a divergent pattern would generate a positive  
 530 (eastward) pressure gradient force over the western section of S3, which drove northward geostrophic flows  
 531 associated with the HSSW transport occupying this area (Figs. 11e, h, k and n).

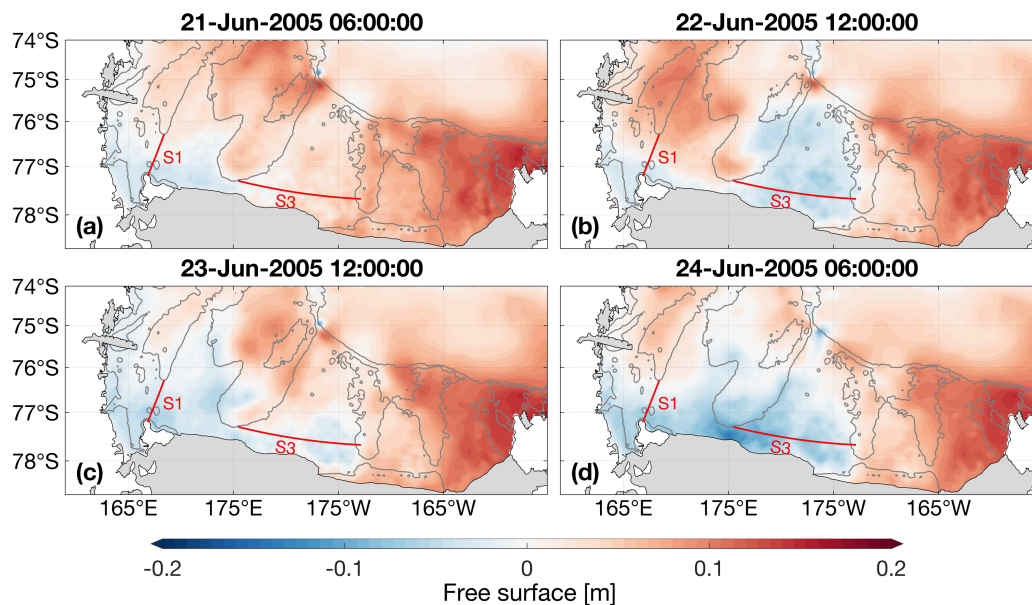
532



533

534 **Figure 13.** (a–t) Vertical sections of the momentum equation terms (Eq. (1)) along S3 at four selected time  
 535 moments during the MESO event (indicated by the magenta triangles in Figs. 11a and 11b): (a, f, k and p)  
 536 local acceleration, (b, g, l and q) Coriolis acceleration, (c, h, m and r) pressure gradient force, (d, i, n and s)  
 537 nonlinear advection and (e, j, o and t) eddy viscosity in the along-shelf momentum budget.

538



539

540 **Figure 14.** (a–d) Spatial distributions of free surface in the Ross Sea region at four selected time moments  
541 of MESO (indicated by the magenta triangles in Figs. 11a and 11b). The red lines indicate the S1 and S3  
542 section, and the gray lines indicate 500 and 1000 m isobaths.

543

### 544 3.5 Lag time for HSSW formation and export

545 The HSSW formation in the RISP demonstrated a near-instantaneous response to the wind change during  
546 the synoptic- and meso-scale cyclone events (Figs. 6, S3 and 10), which could persist for 12–48 hours after  
547 the passage of the cyclones. These features are somewhat different from the HSSW response over the East  
548 Antarctica coastal polynyas as proposed by Wang et al. (2021), which elucidates a lag response of 10–15  
549 days for the HSSW formation to strong wind events in the Prydz Bay and Shackleton polynyas. Such  
550 discrepancy might be related to the polynya extent and local circulations. The RISP has been regarded as  
551 the highest ice production region among the major 13 Antarctic coastal polynyas (Tamura et al., 2008),  
552 suggesting intensified brine rejection that will result in faster production of HSSW. Another factor might  
553 be the local circulation system including the outflow of basal melting water and the circumpolar deep water  
554 (CDW) intrusion processes over these coastal regions. The CDW intrusions and HSSW exports are highly  
555 spatially and temporally correlated on subdaily time scales over the Ross Sea (Morrison et al., 2020), so  
556 the cross-slope transports of CDW could largely modulate the HSSW transport in canyons. Meanwhile, the  
557 increased freshwater from ice shelf melting could pump more CDW into the ice shelf cavities (Jourdain et  
558 al. 2017) and reduce the transport of CDW onto the continental shelf region (Dinniman et al. 2018), which  
559 can further affect the formation of dense shelf water.

560

561 The HSSW export across S3 was positively correlated with wind speed over MESO with a 12-hour lag (Fig.  
562 11b). Furthermore, as mentioned before, such a lag relationship between wind and HSSW was robust over  
563 June–September in 2005 and 2014, while the lag time could vary between 6 hours and 12 hours. Mathiot  
564 et al. (2012) documented a 6-month time lag between the HSSW formation in polynyas (TNB and RISP)  
565 and the HSSW transport across the topographic sills in the Ross Sea. The defined sections across the



566 Drygalski Trough and the Joides Trough in their study were located around 74°S, which is about 330 km  
567 further north than the sections we selected. The lag time between the changes in wind and HSSW exports  
568 is highly dependent on the locations of chosen transects and the spreading rate of HSSW.

569

#### 570 **4 Conclusions**

571 This study investigated the response of sea ice and HSSW formation and export in the Ross Ice Shelf  
572 Polynya to meso- and synoptic-scale cyclones based on a coupled ocean-sea ice-ice shelf Ross Sea model.  
573 For synoptic- and meso-scale cyclones, two and one representative events were respectively selected. When  
574 synoptic-scale cyclones prevailed over this region, the entire RISP was dominated by strong offshore winds,  
575 which resulted in increased SIP rates. During the passage of the mesoscale cyclone, SIP increased rapidly  
576 over the western side of RISP but decreased over the eastern side of RISP, due to changes in the offshore  
577 winds associated with the cyclonic wind field. SIP instantaneously responded to the wind change over the  
578 RISP under both the synoptic-scale and mesoscale cyclones. Enhanced HSSW formation was detected  
579 when there was a notable increase of SIP in RISP, mainly in the western side of RISP, and could persist for  
580 12–48 hours after the passage of the cyclones. For the two synoptic-scale cyclones, the increase in HSSW  
581 formation persisted for about 2 days, while the response of HSSW formation to the mesoscale cyclone had  
582 a shorter lag of about 12–18 hours. The HSSW export across the transect over the Drygalski Trough (S1)  
583 negatively correlated with the meridional wind, while the export across the transect over the Glomar  
584 Challenger Trough (S3) was positively correlated with the wind. The variations of the HSSW export across  
585 S1 and S3 were mainly regulated by the geostrophic currents. Pressure gradients driving the geostrophic  
586 currents were related to gradients in sea surface caused by wind-induced Ekman transports. However, there  
587 might be other factors that affected the hydrography near the Ross Island along the S1 transect. For instance,  
588 the melting beneath the RIS and the intrusion of the circumpolar deep water have impacts on currents in  
589 this region, which deserves future investigations to reveal the different responses for S1 and S3. In addition,  
590 tides could further modulate the export and volume of HSSW in this region (Padman et al. 2009; Wang et  
591 al. 2013), and such effects should be considered by using models including the tides in the future.

592

593

594 Data availability.

595 The model data that support the findings of this study are available at  
596 <https://www.dropbox.com/sh/9ilxwsft080cdds/AABmnhFaMKRu2XL98C4YysXDa?dl=0>. More details  
597 about other observed data are presented in Sect. 2.

598

599 Author contributions.

600 ZZ and XW designed the original ideas presented in this manuscript. ZZ conceived the project of response  
601 of Antarctic coastal polynya processes to strong wind events funded by the Shanghai Science and  
602 Technology Committee. XW conducted the model simulation analysis. W and ZZ wrote the original  
603 manuscript draft. MD conducted the 5-day-average model simulations and XW conducted the 6-hourly  
604 outputs. MD, PU, XL and MZ participated in the result interpretation, manuscript preparation and  
605 improvement. All authors contributed to the article and approved the submitted version.

606

607 Competing interests. The authors declare that there is no conflict of interest.

608



609 Acknowledgements.

610 This work is funded by the National Natural Science Foundation of China (Grant No. 41941008 and  
611 41876221), the Shanghai Science and Technology Committee (Grant No. 20230711100 and Grant No.  
612 21QA1404300), the Impact and Response of Antarctic Seas to Climate Change (Grant 583 No: IRASCC  
613 1-02-01B), the National Key Research and Development Program of China (Grant No. 2019YFC1509102),  
614 the Shanghai Pilot Program for Basic Research - Shanghai Jiao Tong University, and the Shanghai Frontiers  
615 Science Center of Polar (SCOPS). Work of PU and ZZ was supported by the European Union's Horizon  
616 2020 research and innovation framework programme under Grant agreement no. 101003590 (PolarRES  
617 project). PU was also supported by the Academy of Finland (Project 322432).  
618



## 619 References

- 620 Ackley, S. F., Stammerjohn, S., Maksym, T., Smith, M., Cassano, J., Guest, P., Tison, J. L., Delille, B.,  
621 Loose, B., Sedwick, P., Depace, L., Roach, L., and Parno, J.: Sea-ice production and  
622 air/ice/ocean/biogeochemistry interactions in the Ross Sea during the PIPERS 2017 autumn field  
623 campaign, *Ann. Glaciol.*, 61, 181–195, <https://doi.org/10.1017/aog.2020.31>, 2020.
- 624 Arndt, J. E., Schenke, H. W., Jakobsson, M., Nitsche, F. O., Buys, G., Goleby, B., Rebesco, M., Bohoyo,  
625 F., Hong, J., Black, J., Greku, R., Udintsev, G., Barrios, F., Reynoso-Peralta, W., Taisei, M., and Wigley,  
626 R.: The International Bathymetric Chart of the Southern Ocean (IBCSO) Version 1.0—A new  
627 bathymetric compilation covering circum-Antarctic waters, *Geophys. Res. Lett.*, 40, 3111–3117,  
628 <https://doi.org/https://doi.org/10.1002/grl.50413>, 2013.
- 629 Arrigo, K. R. and van Dijken, G. L.: Phytoplankton dynamics within 37 Antarctic coastal polynya systems,  
630 *J. Geophys. Res. Ocean.*, 108, <https://doi.org/10.1029/2002JC001739>, 2003.
- 631 Arrigo, K. R., van Dijken, G., and Long, M.: Coastal Southern Ocean: A strong anthropogenic CO<sub>2</sub> sink,  
632 *Geophys. Res. Lett.*, 35, <https://doi.org/10.1029/2008GL035624>, 2008.
- 633 Barthélemy, A., Goosse, H., Mathiot, P., and Fichet, T.: Inclusion of a katabatic wind correction in a  
634 coarse-resolution global coupled climate model, *Ocean Model.*, 48, 45–54,  
635 <https://doi.org/10.1016/j.ocemod.2012.03.002>, 2012.
- 636 Berliand, M. E.: Determining the net long-wave radiation of the earth with consideration of the effect of  
637 cloudiness. *Izv. Akad. Nauk SSSR, Ser. Geofiz.*, 1, 64–78, 1952.
- 638 Bromwich, D. H.: Mesoscale cyclogenesis over the southwestern Ross Sea linked to strong katabatic winds.  
639 *Mon. Wea. Rev.*, 119, 1736–1753.1991.
- 640 Bromwich, D. H., Carrasco, J. F., Zhong Liu, and Ren-Yow Tzeng: Hemispheric atmospheric variations  
641 and oceanographic impacts associated with katabatic surges across the Ross Ice Shelf, Antarctica, *J.*  
642 *Geophys. Res.*, 98, <https://doi.org/10.1029/93jd00562>, 1993.
- 643 Bromwich, D., Liu, Z., Rogers, A. N., and Woert, M. L. Van: WINTER ATMOSPHERIC FORCING OF  
644 THE ROSS SEA POLYNIA Polynias , or areas of combined open water and thin ice surrounded by  
645 sea and / or land ice , are thought to play important roles in heat transfer from ocean to atmosphere , ice  
646 production , the formation, *Ocean. Ice, Atmos. Interact. Antarct. Continental Margin*, 75, 101–133, 1998.
- 647 Bromwich, D. H., Monaghan, A. J., Manning, K. W., and Powers, J. G.: Real-time forecasting for the  
648 Antarctic: An evaluation of the Antarctic Mesoscale Prediction System (AMPS), *Mon. Weather Rev.*,  
649 133, 579–603, <https://doi.org/10.1175/MWR-2881.1>, 2005.
- 650 Budgell, W. P.: Numerical simulation of ice-ocean variability in the Barents Sea region, *Ocean Dyn.*, 55,  
651 370–387, <https://doi.org/10.1007/s10236-005-0008-3>, 2005.
- 652 Budillon, G., Pacciaroni, M., Cozzi, S., Rivarolo, P., Catalano, G., Ianni, C., and Cantoni, C.: An optimum  
653 multiparameter mixing analysis of the shelf waters in the Ross Sea, *Antarct. Sci.*, 15, 105–118,  
654 <https://doi.org/10.1017/S095410200300110X>, 2003.
- 655 Carrasco, J. F. and Bromwich, D. H.: Mesoscale cyclogenesis dynamics over the southwestern Ross Sea,  
656 Antarctica, 98, <https://doi.org/10.1029/92jd02821>, 1993.
- 657 Carrasco, J. F. and Bromwich, D. H.: Climatological Aspects of Mesoscale Cyclogenesis over the Ross Sea  
658 and Ross Ice Shelf Regions of Antarctica, *Mon. Weather Rev.*, 122, 2405–2425,  
659 [https://doi.org/10.1175/1520-0493\(1994\)122<2405:CAOMCO>2.0.CO;2](https://doi.org/10.1175/1520-0493(1994)122<2405:CAOMCO>2.0.CO;2), 1994.
- 660 Carrasco, J. F., Bromwich, D. H., and Monaghan, A. J.: Distribution and characteristics of mesoscale  
661 cyclones in the Antarctic: Ross Sea eastward to the Weddell Sea, *Mon. Weather Rev.*, 131, 289–301,  
662 [https://doi.org/10.1175/1520-0493\(2003\)131<0289:DACOMC>2.0.CO;2](https://doi.org/10.1175/1520-0493(2003)131<0289:DACOMC>2.0.CO;2), 2003.
- 663 Cheng, Z., Pang, X., Zhao, X., and Stein, A.: Heat flux sources analysis to the Ross Ice Shelf Polynya ice  
664 production time series and the impact of wind forcing, *Remote Sens.*, 11, 8–11,  
665 <https://doi.org/10.3390/rs11020188>, 2019.
- 666 Chenoli, S. N., Turner, J., and Samah, A. A.: A strong wind event on the ross ice shelf, antarctica: A case  
667 study of scale interactions, *Mon. Weather Rev.*, 143, 4163–4180, <https://doi.org/10.1175/MWR-D-15-0002.1>, 2015.
- 668





- 669 Comiso, J.C.: Bootstrap sea ice concentrations from Nimbus-7 SMMR and DMSP SSM/I-SSMIS, Version  
670 3 [Indicate subset used]. NASA National Snow and Ice Data Center Distributed Active Archive Center,  
671 Boulder. <https://doi.org/10.5067/7Q8HCCWS410R>, 2017.
- 672 Comiso, J.C., Gordon, A.L.: Interannual variability in summer sea ice minimum, coastal polynyas, and  
673 bottom water formation in the Weddell Sea. In: Jeffries, M. (Eds.), *Antarctic Sea Ice: Physical Processes,*  
674 *Interactions, and Variability*, vol. 74. American Geophysical Union, Washington, DC, pp. 293–315,  
675 1998.
- 676 Condron, A., Bigg, G. R., and Renfrew, I. A.: Polar mesoscale cyclones in the northeast Atlantic:  
677 Comparing climatologies from ERA-40 and satellite imagery, 134, 1518–1533,  
678 <https://doi.org/10.1175/MWR3136.1>, 2006.
- 679 Dale, E. R., McDonald, A. J., Coggins, J. H. J., and Rack, W.: Atmospheric forcing of sea ice anomalies in  
680 the Ross Sea polynya region, 11, 267–280, <https://doi.org/10.5194/tc-11-267-2017>, 2017.
- 681 Dee, D. P., Uppala, S. M., Simmons, A. J., Berrisford, P., Poli, P., Kobayashi, S., Andrae, U., Balsameda,  
682 M. A., Balsamo, G., Bauer, P., Bechtold, P., Beljaars, A. C. M., van de Berg, L., Bidlot, J., Bormann,  
683 N., Delsol, C., Dragani, R., Fuentes, M., Geer, A. J., Haimberger, L., Healy, S. B., Hersbach, H., Hólm,  
684 E. V., Isaksen, I., Kållberg, P., Köhler, M., Matricardi, M., McNally, A. P., Monge-Sanz, B. M.,  
685 Morcrette, J.-J., Park, B.-K., Peubey, C., de Rosnay, P., Tavolato, C., Thépaut, J.-N., and Vitart, F.: The  
686 ERA-Interim reanalysis: configuration and performance of the data assimilation system, *Q. J. R.*  
687 *Meteorol. Soc.*, 137, 553–597, <https://doi.org/10.1002/qj.828>, 2011.
- 688 Ding, Y., Cheng, X., Li, X., Shokr, M., Yuan, J., Yang, Q., and Hui, F.: Specific Relationship between the  
689 Surface Air Temperature and the Area of the Terra Nova Bay Polynya, Antarctica, *Adv. Atmos. Sci.*,  
690 37, 532–544, <https://doi.org/10.1007/s00376-020-9146-2>, 2020.
- 691 Dinniman, M. S., Klinck, J. M., and Smith, W. O.: A model study of Circumpolar Deep Water on the West  
692 Antarctic Peninsula and Ross Sea continental shelves, *Deep. Res. Part II Top. Stud. Oceanogr.*, 58,  
693 1508–1523, <https://doi.org/10.1016/j.dsr2.2010.11.013>, 2011.
- 694 Dinniman, M. S., Klinck, J. M., Bai, L. S., Bromwich, D. H., Hines, K. M., and Holland, D. M.: The effect  
695 of atmospheric forcing resolution on delivery of ocean heat to the antarctic floating ice shelves, *J. Clim.*,  
696 28, 6067–6085, <https://doi.org/10.1175/JCLI-D-14-00374.1>, 2015.
- 697 Dinniman, M. S., Klinck, J. M., Hofmann, E. E., and Smith, W. O.: Effects of projected changes in wind,  
698 atmospheric temperature, and freshwater inflow on the Ross Sea, *J. Clim.*, 31, 1619–1635,  
699 <https://doi.org/10.1175/JCLI-D-17-0351.1>, 2018.
- 700 Fairall, C. W., Bradley, E. F., Hare, J. E., Grachev, A. A., and Edson, J. B.: Bulk Parameterization of Air–  
701 Sea Fluxes: Updates and Verification for the COARE Algorithm, *J. Clim.*, 16, 571–591,  
702 [https://doi.org/10.1175/1520-0442\(2003\)016<0571:BPOASF>2.0.CO;2](https://doi.org/10.1175/1520-0442(2003)016<0571:BPOASF>2.0.CO;2), 2003.
- 703 Fretwell, P., Pritchard, H. D., Vaughan, D. G., Bamber, J. L., Barrand, N. E., Bell, R., Bianchi, C., Bingham,  
704 R. G., Blankenship, D. D., Casassa, G., Catania, G., Callens, D., Conway, H., Cook, A. J., Corr, H. F.  
705 J., Damaske, D., Damm, V., Ferraccioli, F., Forsberg, R., Fujita, S., Gim, Y., Gogineni, P., Griggs, J.  
706 A., Hindmarsh, R. C. A., Holmlund, P., Holt, J. W., Jacobel, R. W., Jenkins, A., Jokat, W., Jordan, T.,  
707 King, E. C., Kohler, J., Krabill, W., Riger-Kusk, M., Langley, K. A., Leitchenkov, G., Leuschen, C.,  
708 Luyendyk, B. P., Matsuoka, K., Mouginit, J., Nitsche, F. O., Nogi, Y., Nost, O. A., Popov, S. V., Rignot,  
709 E., Rippin, D. M., Rivera, A., Roberts, J., Ross, N., Siegert, M. J., Smith, A. M., Steinhage, D.,  
710 Studinger, M., Sun, B., Tinto, B. K., Welch, B. C., Wilson, D., Young, D. A., Xiangbin, C., and  
711 Zirizzotti, A.: Bedmap2: improved ice bed, surface and thickness datasets for Antarctica, *Cryosph.*, 7,  
712 375–393, <https://doi.org/10.5194/tc-7-375-2013>, 2013.
- 713 Gordon, A.L.; Comiso, J.C.: Polynyas in the southern ocean. *Sci. Am.* 258, 90–97, 1988.
- 714 Haidvogel, D. B., Arango, H., Budgell, W. P., Cornuelle, B. D., Curchitser, E., Di Lorenzo, E., Fennel, K.,  
715 Geyer, W. R., Hermann, A. J., Lanerolle, L., Levin, J., McWilliams, J. C., Miller, A. J., Moore, A. M.,  
716 Powell, T. M., Shchepetkin, A. F., Sherwood, C. R., Signell, R. P., Warner, J. C., and Wilkin, J.: Ocean  
717 forecasting in terrain-following coordinates: Formulation and skill assessment of the Regional Ocean  
718 Modeling System, *J. Comput. Phys.*, 227, 3595–3624, <https://doi.org/10.1016/j.jcp.2007.06.016>, 2008.



- 719 Häkkinen, S. and Mellor, G. L.: Modeling the seasonal variability of a coupled Arctic ice-ocean system, *J.*  
720 *Geophys. Res. Ocean.*, 97, 20285–20304, <https://doi.org/10.1029/92JC02037>, 1992.
- 721 Heinemann, G.: Mesoscale Vortices in the Weddell Sea Region (Antarctica), *Mon. Weather Rev.*, 118,  
722 779–793, [https://doi.org/10.1175/1520-0493\(1990\)118<0779:MVITWS>2.0.CO;2](https://doi.org/10.1175/1520-0493(1990)118<0779:MVITWS>2.0.CO;2), 1990.
- 723 Hoppema, M., Anderson, L.G.: Chapter 6 Biogeochemistry of Polynyas and Their Role in Sequestration of  
724 Anthropogenic Constituents. In: *Polynyas: Windows to the World*. Elsevier Oceanography Series. pp  
725 193–221, 2007.
- 726 Hunke, E. C.: Viscous–Plastic Sea Ice Dynamics with the EVP Model: Linearization Issues, *J. Comput.*  
727 *Phys.*, 170, 18–38, <https://doi.org/10.1006/jcph.2001.6710>, 2001.
- 728 Hunke, E. C. and Dukowicz, J. K.: An Elastic–Viscous–Plastic Model for Sea Ice Dynamics, *J. Phys.*  
729 *Oceanogr.*, 27, 1849–1867, [https://doi.org/10.1175/1520-0485\(1997\)027<1849:AEVPMF>2.0.CO;2](https://doi.org/10.1175/1520-0485(1997)027<1849:AEVPMF>2.0.CO;2),  
730 1997.
- 731 Jacobs, S. S., Amos, A. F., and Bruchhausen, P. M.: Ross sea oceanography and antarctic bottom water  
732 formation, *Deep Sea Res. Oceanogr. Abstr.*, 17, 935–962, [https://doi.org/10.1016/0011-](https://doi.org/10.1016/0011-7471(70)90046-X)  
733 [7471\(70\)90046-X](https://doi.org/10.1016/0011-7471(70)90046-X), 1970.
- 734 Jacobs, S. S., Fairbanks, R. G., and Horibe, Y.: Origin and Evolution of Water Masses Near the Antarctic  
735 continental Margin: Evidence from H218O/H216O Ratios in Seawater, in: *Oceanology of the Antarctic*  
736 *Continental Shelf*, American Geophysical Union (AGU), 59–85, <https://doi.org/10.1029/AR043p0059>,  
737 1985.
- 738 Jendersie, S., Williams, M. J. M., Langhorne, P. J., and Robertson, R.: The Density-Driven Winter  
739 Intensification of the Ross Sea Circulation, *J. Geophys. Res. Ocean.*, 123, 7702–7724,  
740 <https://doi.org/10.1029/2018JC013965>, 2018.
- 741 Jourdain, N. C., Mathiot, P., Merino, N., Durand, G., Le Sommer, J., Spence, P., Dutrieux, P., and Madec,  
742 G.: Ocean circulation and sea-ice thinning induced by melting ice shelves in the Amundsen Sea, 122,  
743 2550–2573, <https://doi.org/10.1002/2016JC012509>, 2017.
- 744 Kern, S.: Wintertime Antarctic coastal polynya area: 1992–2008, *Geophys. Res. Lett.*, 36, 1–5,  
745 <https://doi.org/10.1029/2009GL038062>, 2009.
- 746 Knuth, S. L. and Cassano, J. J.: An analysis of near-surface winds, air temperature, and cyclone activity in  
747 Terra Nova Bay, Antarctica, from 1993 to 2009, *J. Appl. Meteorol. Climatol.*, 50, 662–680,  
748 <https://doi.org/10.1175/2010JAMC2507.1>, 2011.
- 749 Large, W.G., McWilliams, J.C., and Doney, S.C.: Oceanic vertical mixing: A review and a model with  
750 nonlocal boundary layer parameterization. *Rev. Geophys.*, 32, 363–403,  
751 <https://doi.org/10.1029/94RG01872>, 1994.
- 752 Lutgens, F.K., and Tarbuck, E.J.: *The atmosphere*, 8th edn. Prentice Hall, New York, 2001.
- 753 Markus, T. and Cavalieri, D. J.: An enhancement of the NASA Team sea ice algorithm, *IEEE Trans. Geosci.*  
754 *Remote Sens.*, 38, 1387–1398, <https://doi.org/10.1109/36.843033>, 2000.
- 755 Massom, R. A., Harris, P. T., Michael, K. J., and Potter, M. J.: The distribution and formative processes of  
756 latent-heat polynyas in East Antarctica, *Ann. Glaciol.*, 27, 420–426,  
757 <https://doi.org/10.3189/1998AoG27-1-420-426>, 1998.
- 758 Mathiot, P., Barnier, B., Gallée, H., Molines, J. M., Sommer, J. Le, Juza, M., and Penduff, T.: Introducing  
759 katabatic winds in global ERA40 fields to simulate their impacts on the Southern Ocean and sea-ice,  
760 *Ocean Model.*, 35, 146–160, <https://doi.org/10.1016/j.ocemod.2010.07.001>, 2010.
- 761 Mathiot, P., Jourdain, N. C., Barnier, B., Gallée, H., Molines, J. M., Le Sommer, J., and Penduff, T.:  
762 Sensitivity of coastal polynyas and high-salinity shelf water production in the Ross Sea, Antarctica, to  
763 the atmospheric forcing, 62, 701–723, <https://doi.org/10.1007/s10236-012-0531-y>, 2012.
- 764 Mellor, G. L. and Kantha, L.: An ice-ocean coupled model, *J. Geophys. Res. Ocean.*, 94, 10937–10954,  
765 <https://doi.org/10.1029/JC094iC08p10937>, 1989.
- 766 Morales Maqueda, M. A., Willmott, A. J., and Biggs, N. R. T.: Polynya dynamics: A review of observations  
767 and modeling, *Rev. Geophys.*, 42, <https://doi.org/10.1029/2002RG000116>, 2004.



- 768 Morrison, A. K., McC. Hogg, A., England, M. H., and Spence, P.: Warm Circumpolar Deep Water transport  
769 toward Antarctica driven by local dense water export in canyons, 6, 1–10,  
770 <https://doi.org/10.1126/sciadv.aav2516>, 2020.
- 771 Murray, R. J. and Simmonds, I.: A numerical scheme for tracking cyclone centres from digital data. Part I:  
772 development and operation of the scheme, *Aust. Meteorol. Mag.*, 39, 1991.
- 773 Nihashi, S. and Ohshima, K. I.: Circumpolar Mapping of Antarctic Coastal Polynyas and Landfast Sea Ice:  
774 Relationship and Variability, *J. Clim.*, 28, 3650–3670, <https://doi.org/10.1175/JCLI-D-14-00369.1>,  
775 2015.
- 776 Nihashi, S., Ohshima, K. I., and Tamura, T.: Sea-Ice Production in Antarctic Coastal Polynyas Estimated  
777 From AMSR2 Data and Its Validation Using AMSR-E and SSM/I-SSMIS Data, *IEEE J. Sel. Top. Appl.*  
778 *Earth Obs. Remote Sens.*, 10, 3912–3922, <https://doi.org/10.1109/JSTARS.2017.2731995>, 2017.
- 779 Ohshima, K. I., Fukamachi, Y., Williams, G. D., Nihashi, S., Roquet, F., Kitade, Y., Tamura, T., Hirano,  
780 D., Herraiz-Borreguero, L., Field, I., Hindell, M., Aoki, S., and Wakatsuchi, M.: Antarctic Bottom  
781 Water production by intense sea-ice formation in the Cape Darnley polynya, *Nat. Geosci.*, 6, 235–240,  
782 <https://doi.org/10.1038/ngeo1738>, 2013.
- 783 Padman, L., Howard, S. L., Orsi, A. H., and Muench, R. D.: Tides of the northwestern Ross Sea and their  
784 impact on dense outflows of Antarctic Bottom Water, *Deep. Res. Part II Top. Stud. Oceanogr.*, 56, 818–  
785 834, <https://doi.org/10.1016/j.dsr2.2008.10.026>, 2009.
- 786 Parish, T. R. and Cassano, J. J.: The Role of Katabatic Winds on the Antarctic Surface Wind Regime, *Mon.*  
787 *Weather Rev.*, 131, 317–333, [https://doi.org/10.1175/1520-  
788 0493\(2003\)131<0317:TROKWO>2.0.CO;2](https://doi.org/10.1175/1520-0493(2003)131<0317:TROKWO>2.0.CO;2), 2003.
- 789 Petrelli, P., Bindoff, N. L., and Bergamasco, A.: The sea ice dynamics of Terra Nova Bay and Ross Ice  
790 Shelf polynyas during a spring and winter simulation, *J. Geophys. Res. Ocean.*, 113, 1–16,  
791 <https://doi.org/10.1029/2006JC004048>, 2008.
- 792 Powers, J. G., Monaghan, A. J., Cayette, A. M., Bromwich, D. H., Kuo, Y.-H., and Manning, K. W.: Real-  
793 Time Mesoscale Modeling Over Antarctica: The Antarctic Mesoscale Prediction System\*: The  
794 Antarctic Mesoscale Prediction System, *Bull. Am. Meteorol. Soc.*, 84, 1533–1546,  
795 <https://doi.org/10.1175/BAMS-84-11-1533>, 2003.
- 796 Rossow, W. B., Walker, A. W., Beuschel, D. E., and Roiter, M.D.: International Satellite Cloud  
797 Climatology Project (ISCCP) documentation of new cloud datasets. WMO/TD-737, World  
798 Meteorological Organization, 115 pp., [https://isccp.giss.nasa.gov/  
799 pub/documents/d-doc.pdf](https://isccp.giss.nasa.gov/pub/documents/d-doc.pdf), 1996.
- 800 Saunders, P. M., Coward, A. C., and de Cuevas, B. A.: Circulation of the Pacific Ocean seen in a global  
801 ocean model: Ocean Circulation and Climate Advanced Modelling project (OCCAM), *J. Geophys. Res.*  
802 *Ocean.*, 104, 18281–18299, <https://doi.org/10.1029/1999JC900091>, 1999.
- 802 Seefeldt, M. W. and Cassano, J. J.: An analysis of low-level jets in the greater ross ice shelf region based  
803 on numerical simulations, 136, 4188–4205, <https://doi.org/10.1175/2008MWR2455.1>, 2008.
- 804 Shchepetkin, A. F. and McWilliams, J. C.: Correction and commentary for “Ocean forecasting in terrain-  
805 following coordinates: Formulation and skill assessment of the regional ocean modeling system” by  
806 Haidvogel et al., *J. Comp. Phys.* 227, pp. 3595–3624, *J. Comput. Phys.*, 228, 8985–9000,  
807 <https://doi.org/10.1016/j.jcp.2009.09.002>, 2009.
- 808 Simmonds, I.: The climate of the Antarctic region. *Climates of the Southern Continents: Present, Past and*  
809 *Future*, J. E. Hobbs, J. A. Lindesay, and H. A. Bridgman, Eds., John Wiley and Sons, 137–160, 1998.
- 810 Simmonds, I., Keay, K., and Lim, E. P.: Synoptic activity in the seas around Antarctica, *Mon. Weather*  
811 *Rev.*, 131, 272–288, [https://doi.org/10.1175/1520-0493\(2003\)131<0272:SAITSA>2.0.CO;2](https://doi.org/10.1175/1520-0493(2003)131<0272:SAITSA>2.0.CO;2), 2003.
- 812 Stern, A. A., Dinniman, M. S., Zagorodnov, V., Tyler, S. W., and Holland, D. M.: Intrusion of warm surface  
813 water beneath the McMurdo Ice Shelf, Antarctica, *J. Geophys. Res. Ocean.*, 118, 7036–7048,  
814 <https://doi.org/10.1002/2013JC008842>, 2013.
- 815 Stössel, A., Zhang, Z., and Vihma, T.: The effect of alternative real-time wind forcing on Southern Ocean  
816 sea ice simulations, *J. Geophys. Res. Ocean.*, 116, 1–19, <https://doi.org/10.1029/2011JC007328>, 2011.



- 817 Tamura, T., Ohshima, K. I., and Nihashi, S.: Mapping of sea ice production for Antarctic coastal polynyas,  
818 *Geophys. Res. Lett.*, 35, 1–5, <https://doi.org/10.1029/2007GL032903>, 2008.
- 819 Thompson, L., Smith, M., Thomson, J., Stammerjohn, S., Ackley, S., and Loose, B.: Frazil ice growth and  
820 production during katabatic wind events in the Ross Sea, Antarctica, 14, 3329–3347,  
821 <https://doi.org/10.5194/tc-14-3329-2020>, 2020.
- 822 Tortell, P. D., Long, M. C., Payne, C. D., Alderkamp, A.-C., Dutrieux, P., and Arrigo, K. R.: Spatial  
823 distribution of pCO<sub>2</sub>, ΔO<sub>2</sub>/Ar and dimethylsulfide (DMS) in polynya waters and the sea ice zone of the  
824 Amundsen Sea, Antarctica, *Deep Sea Res. Part II Top. Stud. Oceanogr.*, 71–76, 77–93,  
825 <https://doi.org/10.1016/j.dsr2.2012.03.010>, 2012.
- 826 Tremblay, J.E., Smith, W.O.: Chapter 8 Primary Production and Nutrient Dynamics in Polynyas. In:  
827 *Polynyas: Windows to the World*. Elsevier Oceanography Series, pp 239–269, 2007.
- 828 Turner, J., Chenoli, S. N., Abu Samah, A., Marshall, G., Phillips, T., and Orr, A.: Strong wind events in the  
829 Antarctic, *J. Geophys. Res. Atmos.*, 114, <https://doi.org/10.1029/2008JD011642>, 2009.
- 830 Uotila, P., Pezza, A. B., Cassano, J. J., Keay, K., and Lynch, A. H.: A comparison of low pressure system  
831 statistics derived from a high-resolution NWP output and three reanalysis products over the Southern  
832 Ocean, *J. Geophys. Res. Atmos.*, 114, 1–19, <https://doi.org/10.1029/2008JD011583>, 2009.
- 833 Uotila, P., Vihma, T., Pezza, A. B., Simmonds, I., Keay, K., and Lynch, A. H.: Relationships between  
834 Antarctic cyclones and surface conditions as derived from high-resolution numerical weather prediction  
835 data, *J. Geophys. Res. Atmos.*, 116, 1–14, <https://doi.org/10.1029/2010JD015358>, 2011.
- 836 Uotila, P., Vihma, T., and Tsukernik, M.: Close interactions between the Antarctic cyclone budget and  
837 large-scale atmospheric circulation, *Geophys. Res. Lett.*, 40, 3237–3241,  
838 <https://doi.org/10.1002/grl.50560>, 2013.
- 839 Wang, Q., Danilov, S., Hellmer, H., Sidorenko, D., Schröter, J., and Jung, T.: Enhanced cross-shelf  
840 exchange by tides in the western Ross Sea, *Geophys. Res. Lett.*, 40, 5735–5739,  
841 <https://doi.org/10.1002/2013GL058207>, 2013.
- 842 Wang, X., Zhang, Z., Wang, X., Vihma, T., Zhou, M., Yu, L., Uotila, P., and Sein, D. V.: Impacts of strong  
843 wind events on sea ice and water mass properties in Antarctic coastal polynyas, *Clim. Dyn.*, 57, 3505–  
844 3528, <https://doi.org/10.1007/s00382-021-05878-7>, 2021.
- 845 Wenta, M. and Cassano, J. J.: The atmospheric boundary layer and surface conditions during katabatic wind  
846 events over the Terra Nova bay Polynya, *Remote Sens.*, 12, 1–32, <https://doi.org/10.3390/rs12244160>,  
847 2020.
- 848 Weber, N. J., Lazzara, M. A., Keller, L. M., and Cassano, J. J.: The extreme wind events in the Ross Island  
849 region of Antarctica, *Weather Forecast.*, 31, 985–1000, <https://doi.org/10.1175/WAF-D-15-0125.1>,  
850 2016.
- 851 Whitworth III, T., and Orsi, A. H.: Antarctic Bottom Water production and export by tides in the Ross Sea,  
852 *Geophys. Res. Lett.*, 33, <https://doi.org/10.1029/2006GL026357>, 2006.
- 853 Whitworth III, T., Orsi, A.H., Kim, S.J., Nowlin, Jr. W.D., Locarnini, R.A.: Water masses and mixing near  
854 the antarctic slope front. In: *Ocean, ice, and atmosphere: interactions at the Antarctic Continental*  
855 *Margin*, pp 1–27. <https://doi.org/10.1029/AR075p0001>, 2013.
- 856 Yoon, S. T., Sang Lee, W., Stevens, C., Jendersie, S., Nam, S. H., Yun, S., Yeon Hwang, C., Il Jang, G.,  
857 and Lee, J.: Variability in high-salinity shelf water production in the Terra Nova Bay polynya,  
858 Antarctica, *Ocean Sci.*, 16, 373–388, <https://doi.org/10.5194/os-16-373-2020>, 2020.
- 859 Yu, L. and Zhong, S.: Strong wind speed events over Antarctica and its surrounding oceans, *J. Clim.*, 32,  
860 3451–3470, <https://doi.org/10.1175/JCLI-D-18-0831.1>, 2019.
- 861 Zhang, Z., Vihma, T., Stössel, A., and Uotila, P.: The role of wind forcing from operational analyses for  
862 the model representation of Antarctic coastal sea ice, *Ocean Model.*, 94, 95–111,  
863 <https://doi.org/10.1016/j.ocemod.2015.07.019>, 2015.
- 864